PERGAMON

International Journal of Heat and Mass Transfer 43 (2000) 3027–3051

International Journal of
HEAT and MASS TRANSFER

www.elsevier.com/locate/ijhmt

Low-Prandtl number natural convection in volumetrically heated rectangular enclosures
I. Slender cavity, $AR = 4$

Ivan Di Piazza, Michele Ciofalo*

Dipartimento di Ingegneria Nucleare, Università di Palermo, Viale delle Scienze, 90128 Palermo, Italy

Received 5 June 1999; received in revised form 18 November 1999

Abstract

Natural convection in a volumetrically heated rectangular enclosure filled with a low-Prandtl number ($Pr = 0.0321$) fluid was studied by direct numerical two-dimensional simulation. The enclosure had isothermal side walls and adiabatic top/bottom walls. The aspect ratio was 4 and the Grashof number Gr, based on conductive maximum temperature and cavity width, ranged from 3.79×10^4 to 1.26×10^9. According to the value of Gr, different flow regimes were obtained: steady-state, periodic, and chaotic. The first instability of the steady-state solution occurred at $Gr \approx 3 \times 10^5$; the resulting time-periodic flow field consisted of a central rising plume and of convection rolls, periodically generated in the upper corners of the cavity and descending regularly along the vertical isothermal walls. Transition from periodic to chaotic motion occurred at $Gr \approx 1 \times 10^6$; up to the highest Grashof numbers studied, the fluid motion exhibited a recognizable dominating frequency, associated with the process of roll renewal and scaling as $Gr^{1/2}$. The flow field still consisted of a meandering rising plume and of downcoming convection rolls, but these coherent structures were now irregular in shape, size and velocity. For Grashof numbers larger than $\sim 10^6$ (chaotic flow), the friction coefficient averaged along the vertical walls was found to scale as $Gr^{-1/3}$ and the Nusselt number (overall/conductive heat transfer) as $Gr^{1/6}$. © 2000 Elsevier Science Ltd. All rights reserved.

1. Introduction

Studies of free convection in enclosures with internal heat generation have been conducted in the past in connection with such problems as the geophysics of the earth mantle [1] or heat removal from a molten nuclear reactor core [2], and thus have usually focussed on shallow cavities and Prandtl numbers larger than unity. More recently, the problem of free convection with volumetric heat sources has reappeared in connection with advanced engineering applications such as water-cooled lithium–lead breeder blankets for nuclear fusion reactors [3] and liquid metal sources of spallation neutrons for subcritical fission systems [4]. In these latter applications, the Prandtl number is much less than 1 and the geometry is better represented by a slender vertical cavity.

As a preliminary step towards a full understanding of the complex flow occurring in the above and similar configurations, a computational study was conducted of the natural convection flow occurring in a volumetrically heated liquid metal. The value chosen for the Prandtl number, $Pr = 0.0321$, is representative of the

---

* Corresponding author. Tel.: +39-91-232-257; fax: +39-91-232-215.

E-mail address: ciofalo@din.din.unipa.it (M. Ciofalo).

PII: S0017-9310(99)00365-8

Nomenclature

AR	cavity aspect ratio, H/D (–)
C_f	friction coefficient (–)
D	cavity width (m)
F	frequency (s^{-1})
f	dimensionless frequency, F/F_0 (–)
g	acceleration due to gravity (m s^{-2})
Gr	Grashof number, $g\beta qD^5/(k\nu^2) = Ra/Pr$ (–)
H	cavity heigth (m)
k	thermal conductivity (W m^{-1} K^{-1})
Nu_1	first Nusselt number, $1/T_{max}$ (–)
Nu_2	second Nusselt number, $(2/3)/\langle T \rangle$ (–)
P	pressure (N m^{-2})
p	dimensionless pressure, $P/(\rho U_0^2)$ (–)
Pr	Prandtl number, ν/α (–)
q	power density (W m^{-3})
q''	heat flux (W m^{-2})
Ra	Rayleigh number, $g\beta qD^5 Pr/(k\nu^2)$ (–)
t	dimensionless time, τ/τ_0 (–)
T	dimensionless temperature, $(\vartheta - \vartheta_w)/\vartheta_c$ (–)
U, V	velocity components (m s^{-1})
u, v	dimensionless velocities U/U_0, V/U_0 (–)
X, Y	coordinates (m)
x, y	dimensionless coordinates X/D, Y/D (-)

Greek symbols

α	thermal diffusivity (m^2 s^{-1})
β	thermal expansion coefficient (K^{-1})
Δ	mesh size (m)
$\Delta\tau$	time step (s)
δs	dimensionless mesh size, Δ/D (–)
δt	dimensionless time step, $\Delta\tau/\tau_0$ (–)
$\Delta\vartheta$	wall-to-wall temperature drop (K)
ε	dissipation of turbulence energy (W kg^{-1})
ϑ	temperature (K)
ϑ_c	conductive temperature, $(qD^2)/(8k)$ (K)
Λ_K	Kolmogorov dissipative scale, $(\nu^3/\varepsilon)^{1/4}$ (m)
Λ_ϑ	thermal dissipative scale, $(\alpha^3/\varepsilon)^{1/4}$ (m)
ν	kinematic viscosity (m^2 s^{-1})
ρ	density (kg m^{-3})
τ_H	heat diffusive time scale, D^2/α (s)
τ_M	momentum diffusive time scale, D^2/ν (s)
τ	time (s)
$\nabla\vartheta$	vertical temperature gradient (K m^{-1})

Subscripts

BV	Brunt–Väisälä
c	conductive
cr	critical
K	Kolmogorov
min/max	minimum/maximum
P	periodic
w	wall
x, y	directions
0	reference

lithium–lead alloy to be used in the breeder segments of the DEMO nuclear fusion reactor [3]. The computational domain, shown in Fig. 1, was a simple rectangular enclosure with aspect ratio 4, adiabatic top/bottom walls and isothermal side walls.

In particular, the purposes of the study were:

- to determine under which conditions the flow would be steady, unsteady, or chaotic;
- to investigate whether and how the flow would split into separate convection cells or rolls;
- to assess the relative importance of convective heat transfer with respect to conduction.

The cases of square and shallow enclosures will be considered in a companion paper.

2. Literature review

Very few studies, either experimental or computational, have been presented so far on unsteady free convection in liquid metal-filled, volumetrically heated enclosures. However, useful hints can be obtained by studies sharing one or the other aspect with the present problem.

2.1. Internally heated cavities

The free convective flow in horizontal fluid layers with a *large or infinite* planform and internal heat generation has been the subject of many theoretical and experimental investigations. A thorough, but slightly outdated, survey is given by Kulacki and Richards [5].

For a horizontal fluid layer of thickness D with uniform power density q, conductivity k and both walls kept at the same uniform temperature, at sufficiently low value of q heat transfer occurs only by conduction and a parabolic temperature profile is established, with a midplane-to-wall temperature drop $\vartheta_c = (qD^2)/(8k)$. Linear stability theory predicts that the onset of convection occurs at a critical value Ra_{cr} of the Rayleigh number $Ra = g\beta qD^5 Pr/(k\nu^2)$ of ~37,400. Convection presents a cellular planform with downflow in the

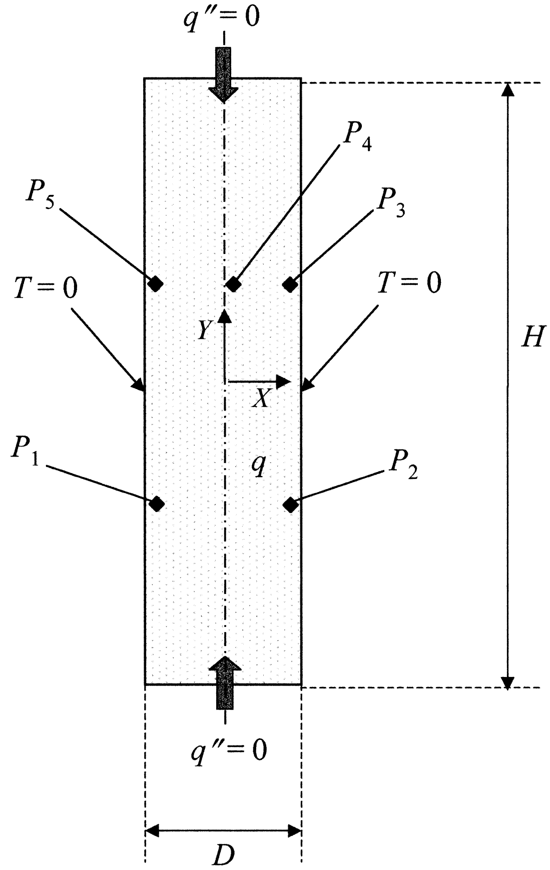

Fig. 1. Sketch of the model rectangular cavity with isothermal vertical walls and adiabatic horizontal walls. The location of monitoring points P1 to P5 is indicated.

centres of cells (unlike Rayleigh–Bènard convection), at least for sufficiently high Prandtl numbers [6]. Cells are stationary up to Rayleigh numbers of $\sim 80 \times Ra_{cr} \approx 3 \times 10^6$, while at higher Ra they become unsteady and chaotic motion occurs.

The problem of an internally heated fluid layer having only the upper boundary at a fixed temperature with the lower boundary adiabatic was studied by Tveitereid and Palm [7]. In this case, linear stability theory predicts the onset of convection at a critical Rayleigh number (defined as above) of 2772. The planform of convection is still characterised by a roughly hexagonal cellular pattern, with downflow in the centres of the cells at Prandtl numbers above 0.25, but upflow at low Pr. Hexagons may become unstable at high $Ra(> 40 \times Ra_{cr})$ in favour of roll-like cells, but some controversy seems to exist on this issue.

As regards enclosures with *finite* planform, most studies have regarded shallow cavities at a Prandtl number of ~3–7, which is easily attainable by using cold water or electrolytes as the simulating fluid. Shallow cavities cooled only from the upper surface were experimentally studied by different authors [8–10]. Transition from laminar to turbulent convection was reported to occur for $Ra > \sim 10^7$, and well mixed temperature distributions were found at higher Rayleigh numbers. However, the Nusselt number was found to increase as $Ra^{0.23-0.24}$ (a typically laminar behaviour) in the whole range $Ra = 10^3$–10^{12}.

Turning to computational studies, Churbanov et al. [11] used two-dimensional direct simulation (with the Navier–Stokes equations recast in ψ–ω form) to compute flow and heat transfer in an internally heated shallow rectangular cavity (aspect ratio $AR = 0.25$–1) at Rayleigh numbers in the range 10^5–10^8 and $Pr = 7$. They tested alternative thermal boundary conditions (including the case of all walls isothermal, a configuration with isothermal horizontal and adiabatic side walls, and a variant with isothermal top and insulated other surfaces) and obtained symmetry-breaking and time-periodic unsteady solutions, although the computational grids used were relatively coarse (e.g., 40×80 nodes).

Daniels and Jones [12] presented a computational study for a shallow cavity with uniform volumetric heating, isothermal side walls and adiabatic top and bottom walls. The authors used a matched asymptotic expansion method valid for Rayleigh numbers (based on the cavity height) of the order $1/AR$. Shallow rectangular cavities ($AR = 0.5$) with isothermal side walls and adiabatic top–bottom walls were also studied by Farouk [13] for $Pr = 6.5$; he used the k–ε turbulence model for Ra in the range 2×10^6–2×10^9, so that the flow unsteadiness was not explicitly simulated, and adopted a time-marching approach to the final steady state. He obtained solutions which exhibited left–right symmetry breaking.

Dinh and co-workers [14–16] simulated flow and heat transfer in a rectangular or hemispherical "corium" pools for Rayleigh numbers up to $\sim 10^{14}$ and $Pr = 3$–7. They assessed alternative turbulence models against direct simulation results and available experimental heat transfer data, and selected a purposely adapted low-Reynolds number k–ε model as that giving the best agreement with the measurements.

May [17] presented a two-dimensional computational study of free convection in a square enclosure of side length D with internal heat generation, inclined at arbitrary angles with respect to the horizontal. All four walls were assumed to be isothermal, the Prandtl number was 7, and the Rayleigh number (once defined as above) ranged from 6.4×10^5 to 9.6×10^6. For a horizontal cavity, May obtained oscillating periodic solutions at $Ra > 3.2 \times 10^6$, but only when the full cavity was simulated without left–right symmetry assumptions. At $Ra = 6.4 \times 10^6$, the period of the oscillation was $\sim 0.38(D^2/\nu)$. The computational grids used were relatively coarse (61×61 cells at most) and a significant residual grid dependence was still present in the results. Numerical predictions were also compared with experimental heat transfer and temperature distribution measurements conducted by Lee and Goldstein [18] using interferometry in a saline water-filled enclosure. A good agreement was reported as regards flow patterns and maximum temperatures in the enclosure, with some disagreement in the heat flux distributions along the walls at the lowest inclination angles (0–15°).

The *simultaneous* presence of internal heat generation and differential wall heating in enclosures has also been the subject of some studies, e.g. [19–21], all of which regard $Pr > 0.7$ and steady-state conditions.

2.2. Related work

Low Prandtl number free convective flows have been the subject of a vast number of studies. Most of them have regarded differentially heated cavities without internal heat generation, conditions which are quite removed from those investigated in the present work. However, some of the main findings, notably regarding flow regimes and their transitions, deserve a brief survey here.

For differentially heated fluid layers with a wall-to-wall temperature difference $\Delta\vartheta$, the Rayleigh number is usually defined as $Ra = g\beta\Delta\vartheta D^3 Pr/\nu^2$. This can be compared with the definition given above for internally heated fluid layers by observing that, in the latter case, a natural temperature scale is the purely conductive temperature drop ϑ_c which, according to the thermal boundary conditions, is given by $\vartheta_c = qD^2/(8k)$ (both main walls isothermal at the same temperature) or by $\vartheta_c = qD^2/(2k)$ (one of the main walls isothermal, the opposite adiabatic).

For shallow enclosures ($AR < 1$), in the limit of low Rayleigh number, two-dimensional flow and infinite horizontal extent, an analytical solution (Hadley-cell flow) exists. Braunsfurth et al. [22] found by experiments and two-dimensional finite element simulations that, for $Pr \approx 0.025$ (liquid gallium), as the Rayleigh number increases from 1.6×10^5 to 8×10^5, a progressive departure from the Hadley-cell solution is observed; the two-dimensional laminar steady solution is stable to two-dimensional disturbances and no Hopf bifurcation to oscillating behaviour occurs. However, previous studies conducted at lower Pr [23] had shown that a Hopf bifurcation does occur, e.g. for $Ra = 36{,}500$ at $Pr = 0.015$ and for $Ra/Pr \rightarrow 1.63 \times 10^6$ at $Pr \rightarrow 0$.

Coarse-mesh three-dimensional finite-difference simulations of free convection of gallium ($Pr = 0.027$) in rectangular enclosures of different aspect ratios were presented by Viskanta et al. [24] and were compared with experimental temperature distributions. The Rayleigh number was $\sim 10^6$. At this Ra, the flow was found to be steady and laminar. The authors observed that three-dimensional effects were significant and, due to the low value of the Prandtl number, extended down to the mid-plane of the cavity instead of being confined to the front and back walls. Also, a correct modelling of the thermal boundary conditions was found to be crucial.

3. Model

As mentioned in Section 1, the physical model adopted in the present study consists of a rectangular, vertical, fluid-filled cavity of height H and width D. Fig. 1 reports also the location of five monitoring points (used in the following). The fluid motion is driven by a uniform internal power density q, the left and right walls being at constant temperature, ϑ_w and the upper and lower boundaries at zero heat flux. The fluid considered is a liquid metal (Li–17Pb alloy), characterized by a Prandtl number of 0.0321 at 300°C.

In order to write the governing equations in dimensionless form, it is necessary to introduce appropriate scales for length, temperature, time, velocity and pressure. The most natural length scale is D, the distance between the isothermal walls. For temperature, the conductive scale $\vartheta_c = qD^2/(8k)$ was chosen here; it represents the midplane-to-wall temperature drop in the absence of convection. As regards the frequency or time scales, by analogy with the previously defined Brunt–Väisälä frequency F_{BV}, which characterizes stably-stratified flows, one may introduce a reference frequency $F_0 = (g\beta\vartheta_c/D)^{1/2}/(2\pi)$. The corresponding time scale is $\tau_0 = F_0^{-1}$, which may be written as $\tau_0 = (4\pi\sqrt{2}Gr^{-1/2})\tau_M$, $\tau_M = D^2/\nu$ being the momentum diffusive time scale and $Gr = g\beta qD^5/(k\nu^2) = Ra/Pr$ the Grashof number. A velocity scale coherent with the above definitions is $U_0 = D/\tau_0$, i.e. the ratio of length to time scales. Finally, an appropriate pressure scale is ρU_0^2. As confirmed a posteriori by the computational results, the above choice of scales allowed all variables to remain in unity order throughout the range of parameters investigated.

The two-dimensional continuity and momentum equations, coupled with the energy transport equation under the Boussinesq approximation, may be written in dimensionless form as:

$$\frac{\partial u}{\partial x} + \frac{\partial v}{\partial y} = 0 \qquad (1)$$

$$\frac{\partial u}{\partial t}+u\frac{\partial u}{\partial x}+v\frac{\partial u}{\partial y}=-\frac{\partial p}{\partial x}+\frac{4\pi\sqrt{2}}{\sqrt{Gr}}\left(\frac{\partial^2 u}{\partial x^2}+\frac{\partial^2 u}{\partial y^2}\right) \tag{2a}$$

$$\frac{\partial v}{\partial t}+u\frac{\partial v}{\partial x}+v\frac{\partial v}{\partial y} =-\frac{\partial p}{\partial y}+\frac{4\pi\sqrt{2}}{\sqrt{Gr}}\left(\frac{\partial^2 v}{\partial x^2}+\frac{\partial^2 v}{\partial y^2}\right)+4\pi^2 T \tag{2b}$$

$$\frac{\partial T}{\partial t}+u\frac{\partial T}{\partial x}+v\frac{\partial T}{\partial y}=\frac{4\pi\sqrt{2}}{\sqrt{Gr}\cdot Pr}\left(\frac{\partial^2 T}{\partial x^2}+\frac{\partial^2 T}{\partial y^2}+8\right) \tag{3}$$

in which $x=X/D$, $y=Y/D$, $u=U/U_0$, $v=V/U_0$, $p=P/(\rho U_0^2)$, $T=(\vartheta-\vartheta_w)/\vartheta_c$, $t=\tau/\tau_0$. The boundary conditions are:

$$u=v=0,\quad \partial T/\partial y=0 \quad \text{for} \quad y=\pm AR/2 \tag{4}$$

$$u=v=0,\quad T=0 \quad \text{for} \quad x=\pm 1/2 \tag{5}$$

The Grashof numbers investigated ranged from $\sim 3.79\times 10^4$ to 1.26×10^9.

In the limit of infinitely slender cavity (parallel flow) and under the assumption of steady-state conditions, Eqs. (1)–(3) with boundary conditions (5) can be given a simple analytical solution [5]. By assuming $\partial v/\partial y=\partial T/\partial y=0$, it follows from continuity that $u=0$; moreover, all convective terms vanish, $\partial p/\partial x=0$ and Eqs. (1)–(3) are reduced to:

$$0=-\frac{\mathrm{d}p}{\mathrm{d}y}+\frac{4\pi}{\sqrt{Gr/2}}\cdot\frac{\mathrm{d}^2 v}{\mathrm{d}x^2}+4\pi^2 T \tag{6}$$

$$0=\frac{4\pi}{\sqrt{Gr/2}\cdot Pr}\cdot\left(\frac{\mathrm{d}^2 T}{\mathrm{d}x^2}+8\right) \tag{7}$$

with boundary conditions $v=T=0$ for $x=\pm 1/2$. The solution to Eqs. (6) and (7) is:

$$v=\pi\sqrt{\frac{Gr}{2}}\cdot\left(\frac{x^4}{3}-\frac{x^2}{10}+\frac{1}{240}\right) \tag{8}$$

$$T=1-4x^2 \tag{9}$$

Note that the dimensionless temperature distribution follows the pure conductive behaviour independent of the Prandtl and Grashof numbers, and that the dimensionless velocity distribution depends only on the Grashof number. The wall shear stress, once made dimensionless with respect to ρU_0^2, i.e. expressed as a friction coefficient C_f, is given by $C_f=4\pi^2/15\approx 2.63$ and does not depend on Gr. The $Gr^{1/2}$ dependence of the (dimensionless) velocity v reflects the fact that, as far as the end regions are neglected, the temperature distribution is unaffected by convection and the fluid velocity is given by a balance of viscous forces and *constant* buoyancy forces, yielding (dimensional) velocities proportional to q (i.e., to Gr).

Under the same assumption of parallel flow, in the case of a differentially heated, infinitely long horizontal container with adiabatic top and bottom walls, a similar steady-state solution (Hadley cell) exists [22].

4. Numerical methods

Eqs. (1)–(3) were solved by using a finite-volume technique based on the SIMPLEC pressure–velocity coupling algorithm [25], Crank–Nicholson time stepping and the central discretization scheme for the diffusive and advective terms. At each step, the SIMPLEC algorithm was iterated until the mass, momentum and enthalpy residuals exhibited no further reduction; this typically required 20 to 50 iterations.

As will be discussed in the following sections, according to the Grashof number the flow either attained a steady-state configuration or exhibited periodic or chaotic unsteadiness. In the former case ($Gr\le 3\times 10^5$), the simulation was protracted until no significant variation of monitored quantities was observed. This typically required about 10 conductive time constants $\tau_H=D^2/\alpha$, corresponding to a dimensionless duration increasing from ~ 1.6 for $Gr=3.79\times 10^4$ (lowest Grashof number simulated) to ~ 4 for $Gr=2.19\times 10^5$ (highest Grashof number for which a steady-state solution was attained). In the cases with time-dependent behaviour, as will be discussed in detail in the following sections, the flow exhibited a dominating period ranging from ~ 3 to 6 (τ_0 units). Simulations were protracted in most cases so as to include at least six such periods, i.e. for a dimensionless time $t_{\max}$ of ~ 20–40.

In the case of chaotic flow (which was obtained here for $Gr\ge 10^6$), the main criterion for the choice of the computational grid is that all relevant (energy-containing) time-dependent flow structures ("eddies") are properly resolved. This requires the mesh size Δ to be of the same order as the Kolmogorov scale Λ_K of dissipative eddies. This can be expressed [26] as:

$$\Lambda_K=\left(v^3/\varepsilon\right)^{1/4} \tag{10}$$

in which ε is the rate of dissipation of *turbulence* energy per unit mass (p.u.m.). The *total* rate of dissipation p.u.m. of mechanical energy in the cavity can be estimated as the product of the buoyancy acceleration, $\sim g\beta\vartheta_c$, by the buoyant velocity, $\sim U_0=D/\tau_0$. In fully chaotic flow, most of the dissipation occurs through a cascade of turbulent structures so that one can write:

$$\varepsilon \approx g\beta\vartheta_c D/\tau_0 \qquad (11)$$

By substituting Eq. (11) for ε into Eq. (10) and taking the definitions of ϑ_c, Gr and τ_0 into account, the following estimate is obtained for the dimensionless dissipative scale $\lambda_K = \Lambda_K/D$:

$$\lambda_K \approx \left(32\pi\sqrt{2}\right)^{1/4} Gr^{-3/8} \qquad (12)$$

This can be used as an estimate of the maximum dimensionless mesh size $\delta s = \Delta/D$. For example, Eq. (12) gives $\lambda_K \approx 0.02$ for $Gr = 10^6$ and $\lambda_K \approx 0.004$ for $Gr = 10^8$, suggesting that ~50 × 200 cells would be required for the present aspect ratio of 4 in the former case and ~250 × 1000 cells in the latter.

Of course, the dissipative scale of thermal structures is larger than the above scale of the mechanical structures since it can be expressed as $\Lambda_\vartheta = Pr^{-3/4}\Lambda_K$ (yielding $\Lambda_\vartheta \approx 13\Lambda_K$ for the present Prandtl number of 0.0321).

As regards the time step, the implicit (Crank–Nicholson) time stepping scheme adopted in the present simulations imposes no stability requirements. However, in chaotic flow simulations, the time scale of dissipative (Kolmogorov) eddies must be resolved. By adopting Taylor's hypothesis of "frozen turbulence" and remembering that the typical dimensionless convective velocity is of unity order, the requirement on the time step δt can be made formally identical to the spatial resolution requirement on the mesh size δs, expressed by Eq. (12). Therefore, one may write:

$$\delta t \approx \delta s \approx \lambda_K \qquad (13)$$

Although the "frozen turbulence" hypothesis can hardly be regarded as rigorous for the present, confined-convection, flow, yet it is coherent with the Eulerian representation underlying the description of the problem. Of course, the criteria expressed by Eqs. (12) and (13) become meaningless out of the range of the cases exhibiting chaotic behaviour, i.e. at $Gr < \sim 10^6$.

Unfortunately, a strict observance of the above criteria was computationally prohibitive. The computational grids used in this study had up to 128 × 220 ($N_x \times N_y$) nodes, selectively refined in the wall region by using a geometrical progression with $\Delta_{\max}/\Delta_{\min} = 60$. For $Gr > 10^7$, complete grid independence could not be demonstrated; for example, at $Gr = 3.79 \times 10^8$ the mean wall friction coefficient changed by 4% as the grid was refined from 50 × 100 to 128 × 220 nodes. However, in view of the main purposes of the present study (which were to investigate the qualitative behaviour of the flow and to identify the most relevant phenomena involved, rather than to draw detailed quantitative estimates), this degree of grid independence was accepted as satisfactory.

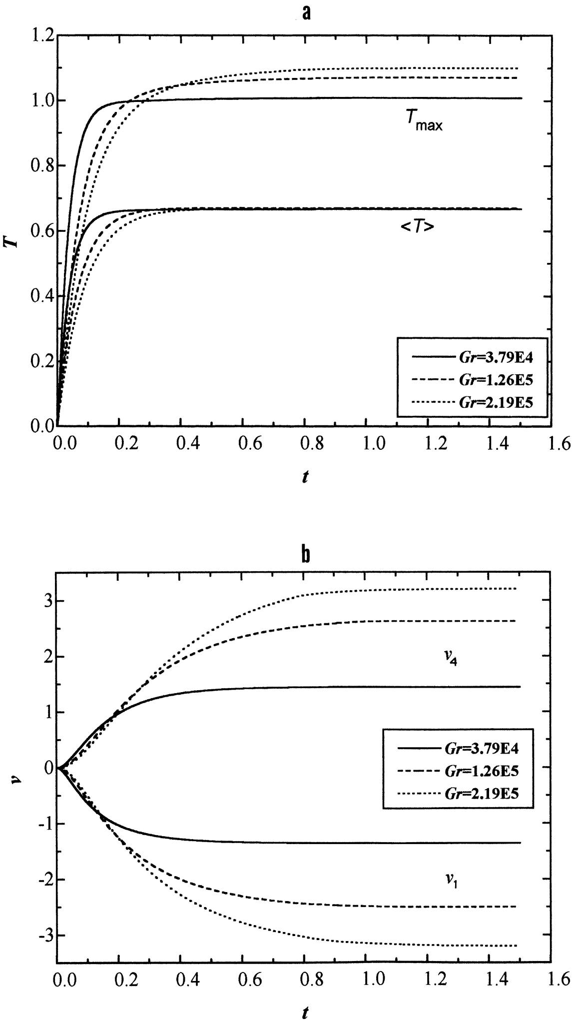

Fig. 2. Initial transient for cases attaining a steady-state condition. (a) Average and maximum temperatures; (b) vertical velocity at monitoring points 1 and 4.

As regards the time step, in most cases it was set to 4×10^{-3} (in dimensionless form), which implies that — in the case of unsteady flow — a main period was resolved by 750 to 1500 steps. Simulations repeated by halving this value showed no significant change in the case of steady-state or periodic flow, and no *statistically* significant change in the case of chaotic flow. In all cases, the "natural" initial conditions $u = v = T = 0$ were adopted; no disturbance was explicitly superimposed on the flow or thermal fields, so that, whenever spatial symmetry breaking occurred, this was only due to the growth of small asymmetric numerical errors in the solution.

Each simulation typically required 45–180 s per time

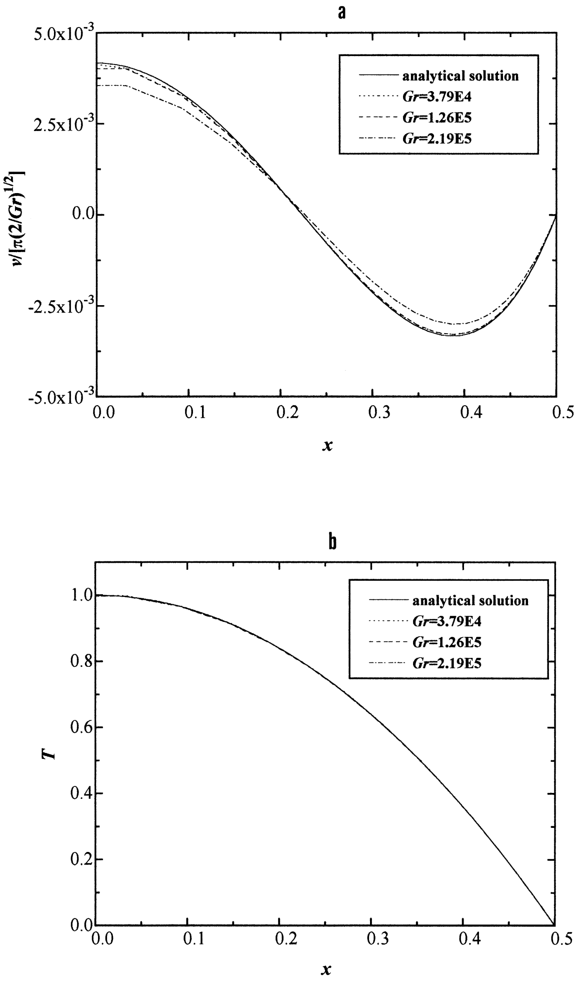

Fig. 3. Profiles of (a) scaled vertical velocity and (b) temperature at mid height ($y = 0$) for the steady-state cases. Solid line: asymptotic slender cavity solution; broken lines: numerical results for different Grashof numbers.

step (according to the computational grid used) on a Pentium-II 350 MHz computer with 128 Mb RAM.

Most of the results will be presented in the form of time series of computed quantities at monitoring points or of whole-field maps of streamlines, isotherms or derived quantities. In addition to these, the *Eulerian time power spectrum* can be computed for each point quantity $\phi(t)$ as:

$$P_{\phi\phi}(f) = |\int_{t_{\min}}^{t_{\max}} \phi(t) \cdot e^{2\pi jft}\, \mathrm{d}t|^2 \tag{14}$$

The Fast Fourier Transform algorithm was used here

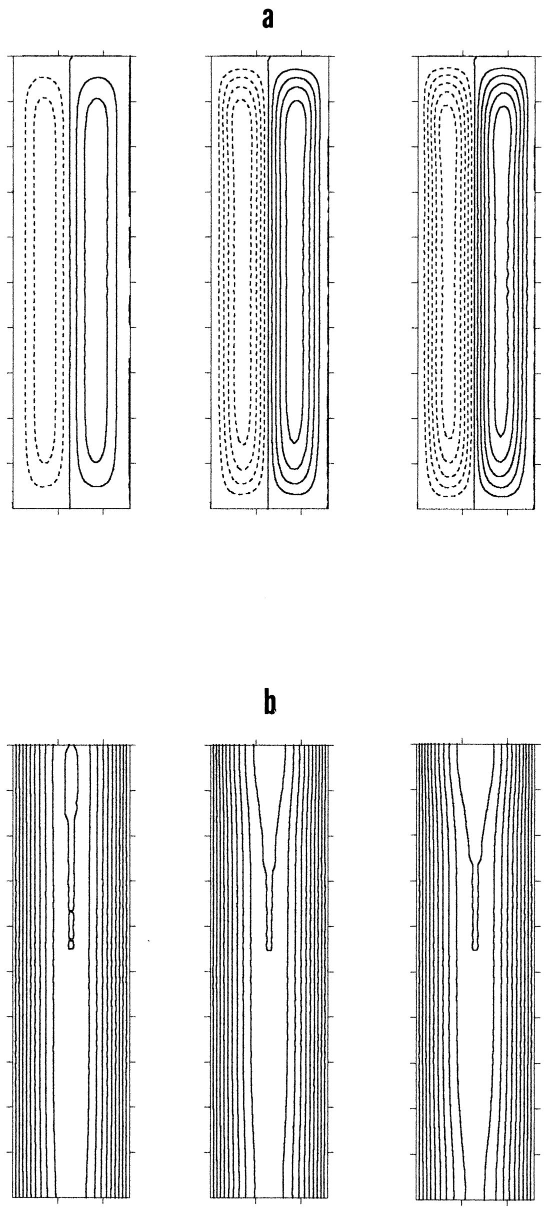

Fig. 4. Predicted flow and temperature fields for the steady-state cases. From left to right: $Gr = 3.79 \times 10^4$, 1.26×10^5 and 2.19×10^5. (a) Streamlines, dimensionless separation = 0.2. Solid lines: clockwise flow; broken lines: anti-clockwise flow. (b) Isotherms, dimensionless separation = 0.1.

to evaluate $P_{\phi\phi}$. Corresponding spectra start from a minimum frequency $f_{\min} = (t_{\max} - t_{\min})^{-1}$, and include values of $P_{\phi\phi}$ only at frequencies multiple of $f_{\min}$, up to a maximum value $f_{\max} = (2\delta t)^{-1}$.

5. Steady-state flow

For $Gr \leq 3 \times 10^5$, the flow settled to steady-state solutions. The behaviour of some quantities during the initial transient is shown in Fig. 2 for the three lowest Grashof number cases simulated ($Gr \approx 3.79 \times 10^4$, 1.26×10^5 and 2.19×10^5).

Fig. 2(a) reports average and maximum temperatures as functions of time. The initial temperature rate of rise in the cavity is identical for any point, and is given — in dimensionless terms — by $\partial T/\partial t|_{\text{init}} = 32\pi\sqrt{2}/(Pr\sqrt{Gr})$, as can be deduced from Eq. (3) for initially negligible convection and diffusion. Therefore, in the dimensionless form used here, the initial temperature slope decreases with increasing Gr.

Fig. 2(b) reports the vertical velocity v at two of the monitoring points indicated in Fig. 1 (P_1 and P_4) as a function of time. The increase of v_1 (dimensionless) with Gr is due to the same reasons discussed in Section 3 in relation to the asymptotic slender cavity solution. Note that velocities are still evolving at $t \approx 1$, while, due to the low Prandtl number, temperatures settle to a steady-state value more rapidly ($t \approx 0.5$).

The steady-state numerical solutions are compared with the parallel-flow solution in Fig. 3. Profiles of vertical velocity v (a) and temperature T (b) at the cavity midheight $y = 0$ are compared with the analytical profiles given by Eqs. (7) and (8). The dimensionless velocity v was further scaled by $\pi(2/Gr)^{1/2}$ in order to eliminate most of the Grashof number-dependence of the results. It can be observed that the numerical solution progressively departs from the analytical one as Gr increases but is still close to it at the highest Grashof numbers for which a steady-state solution exists. The temperature profile practically coincides with the purely conductive solution through the whole range of steady-state cases.

Fig. 4 reports steady-state stream function and temperature fields for the three cases. The stream function is made dimensionless with respect to $DU_0 = D^2/\tau_0$. There is only one circulation cell in each half of the cavity, with a perfect left–right symmetry and an approximate up–down symmetry. The temperature fields appear to be only slightly modified with respect to the one-dimensional pure conductive solution. The upwelling stream located around the cavity midline provides convective transport of hot fluid from bottom to top, causing an increase in temperature in the upper–central zone which is more marked at higher Gr, as is reflected by the $T_{\max}$ asymptotic values in Fig. 2(a). Thus, vertical transport breaks the top–bottom symmetry of the purely conductive solution. However, the effect of convection is only to change the temperature distribution without significantly altering its average which remains close to the conductive solution ($\langle T \rangle = 2/3$ in dimensionless terms)[1]. Thus, for the present low Prandtl number, the contribution of convection to overall heat transfer is negligible up to $Gr \approx 3 \times 10^5$ (see also Section 11).

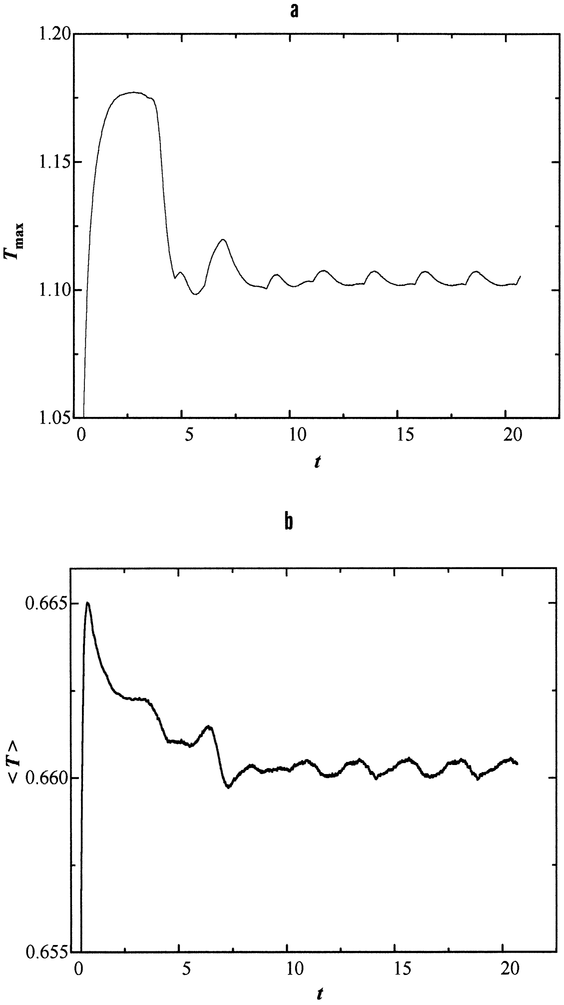

Fig. 5. Behaviour of (a) maximum and (b) average temperatures as functions of time for $Gr = 3.79 \times 10^5$ (periodic flow).

6. Periodic flow

For Grashof numbers ranging approximately from 3×10^5 to 10^6 perfectly periodic solutions were obtained. Note that this range of Gr is similar to that (4.5×10^5–1.35×10^6) for which periodic solutions were obtained by May [17], despite the considerably different Prandtl

---

[1] Throughout this paper, brackets $\langle \bullet \rangle$ are used to denote spatial averaging, while an overbar $\bar{\bullet}$ is used to denote time-averaging.

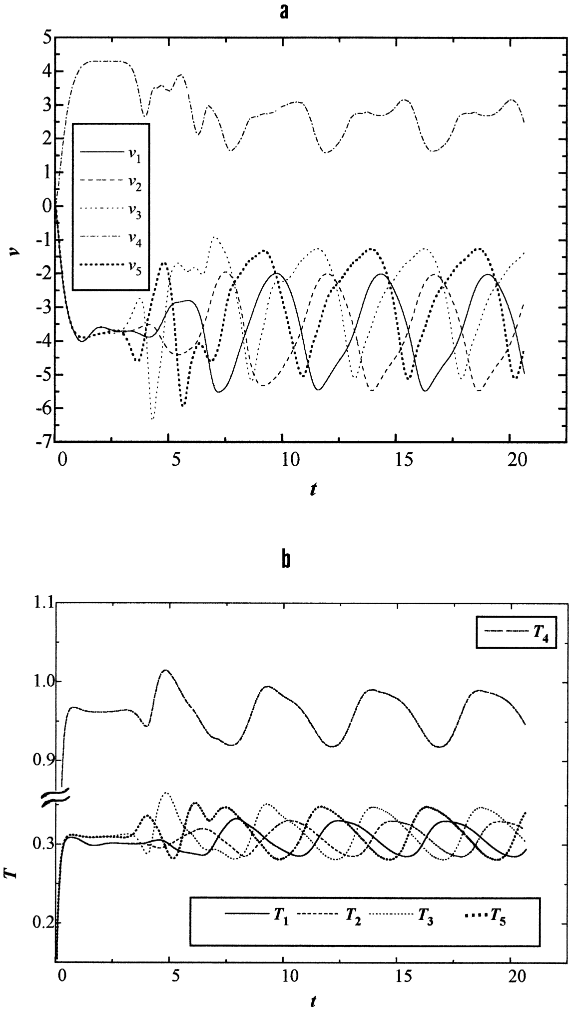

Fig. 6. Behaviour of (a) vertical velocity v and (b) temperature T at monitoring points 1–5 for $Gr = 3.79 \times 10^5$ (periodic flow).

number (7), aspect ratio (1) and thermal boundary conditions (all four walls isothermal).

Two cases were simulated in the periodic range, namely, $Gr = 3.79 \times 10^5$ and 7.03×10^5. Fig. 5 shows the behaviour of maximum and average temperatures as functions of time for the case at lower Gr (3.79×10^5). For the same Gr, Fig. 6 reports the time behaviour of (a) vertical velocity v and (b) temperature T in some of the monitoring points indicated in Fig. 1. Points P_1–P_2 and P_3–P_5 are symmetrically located with respect to the vertical midline; points P_1–P_2 lie in the lower half of the cavity while points P_3–P_5 in the upper half.

The first noteworthy feature of Fig. 6 is that, after a few (~3) time units, the symmetric solution breaks down as instabilities grow, and the time behaviours of quantities relative to geometrically symmetric points begin to differ. The symmetry breaking of the instantaneous flow field occurs almost at the same instant in the upper and lower parts of the cavity (points P_1–P_2, P_3–P_5). A reduction in the temperature maximum is observed following the symmetry breaking (Fig. 5, dimensionless time $t \approx 3$). Starting from 10 time units, quantities at monitoring points exhibit a clearly periodic behaviour, the period being about 4.7 time units. Points that are symmetric in space (P_1–P_2 and P_3–P_5) exhibit the same behaviour, but shifted in time by half a period. Note that the period in the maximum and average temperatures (Fig. 5) is only half of the true period of the solution (Fig. 6); the reason is that the location of the maximum temperature shifts its position with time around the cavity centreline twice in a period, and the average temperature is obviously insensitive to the solution parity.

Fig. 7 reports instantaneous streamlines (a) and isotherms (b) for the same Grashof number (3.79×10^5) during the initial transient. The interval between consecutive plots is ~0.63 in dimensionless form. The figure shows clearly that the break-up of the symmetric steady-state solution occurs at $t \approx 3.5$ (between fifth and sixth frame), after a pseudo-stationary regime has been attained, and is due to the growth of lateral oscillations of wavelength $\lambda \approx D$ in the central rising plume, which results in the appearance of separate downcoming recirculation rolls.

The instability can be interpreted as the growth of an antisymmetric vertical velocity disturbance propagating downwards as a travelling wave with a dimensionless wavenumber of ~1 and a dimensionless speed of ~0.2. A linear stability analysis conducted for the infinite-aspect ratio vertical slot (parallel flow) by Gershuni and co-workers — as reported in Kulacki and Richards [5] — gave a critical Grashof number of ~1 × 10^5 for the growth of antisymmetric travelling-wave disturbances at Prandtl numbers comparable with that of the present study. The associated wavenumber and wave speed were ~0.65 and 0.28, respectively, in the present dimensionless formulation. Both the larger critical Gr and the larger wavenumber observed in the present case for the developed disturbance may be explained by the finite height of the enclosure; interestingly, the dimensionless frequency of the disturbances (wavenumber × speed) is very close to that predicted by the linear stability theory for infinite AR (~0.2).

Fig. 8 shows a time sequence of instantaneous stream function (a) and temperature (b) during one period, after the periodic regime has been attained ($t \approx 15.7$ to 20.1, separation of plots ~0.63). A multicellular asymmetric instantaneous structure is revealed by the graphs relative to the stream function (a), with at least three convection rolls for each side of the cav-

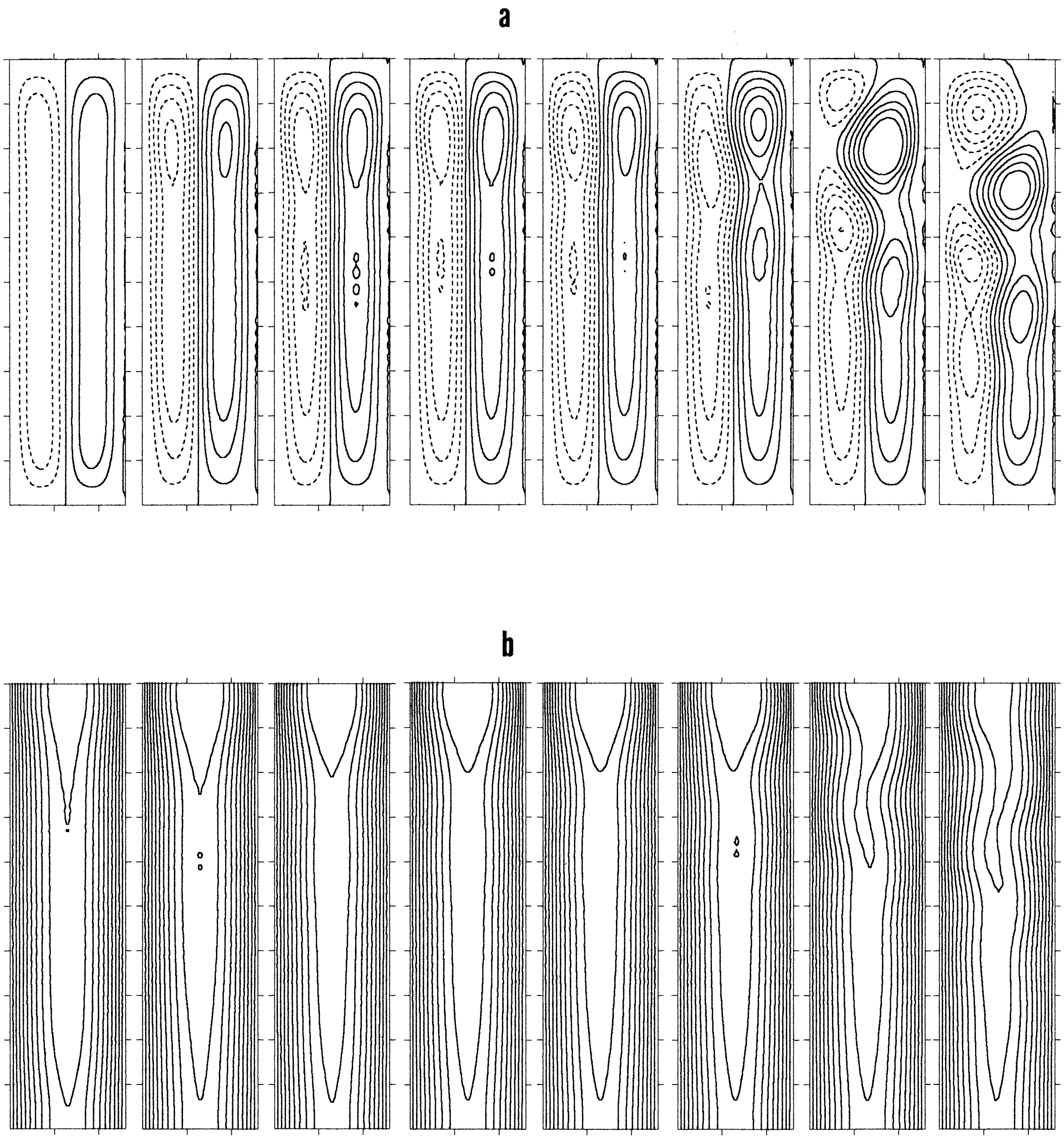

Fig. 7. Initial transient for $Gr = 3.79 \times 10^5$ (periodic flow). Dimensionless time interval between frames ~0.63. (a) Streamlines, dimensionless separation = 0.2. Solid lines: clockwise flow; broken lines: anti-clockwise flow. (b) Isotherms, dimensionless separation = 0.1.

ity. They are alternately disposed in a chessboard fashion at the two sides of the central rising plume. In the instantaneous temperature field (b), the winding shape of the isothermal lines is still recognizable but, as compared to the shape of the null streamline in graphs (a), the amplitude of the lateral oscillation is greatly attenuated by conduction effects which dominate at low Prandtl number.

Anti-clockwise and clockwise convection rolls are generated in the upper left and right corners, respectively; two staggered trains of rolls proceed downward through the cavity and extinguish their energy by vis-

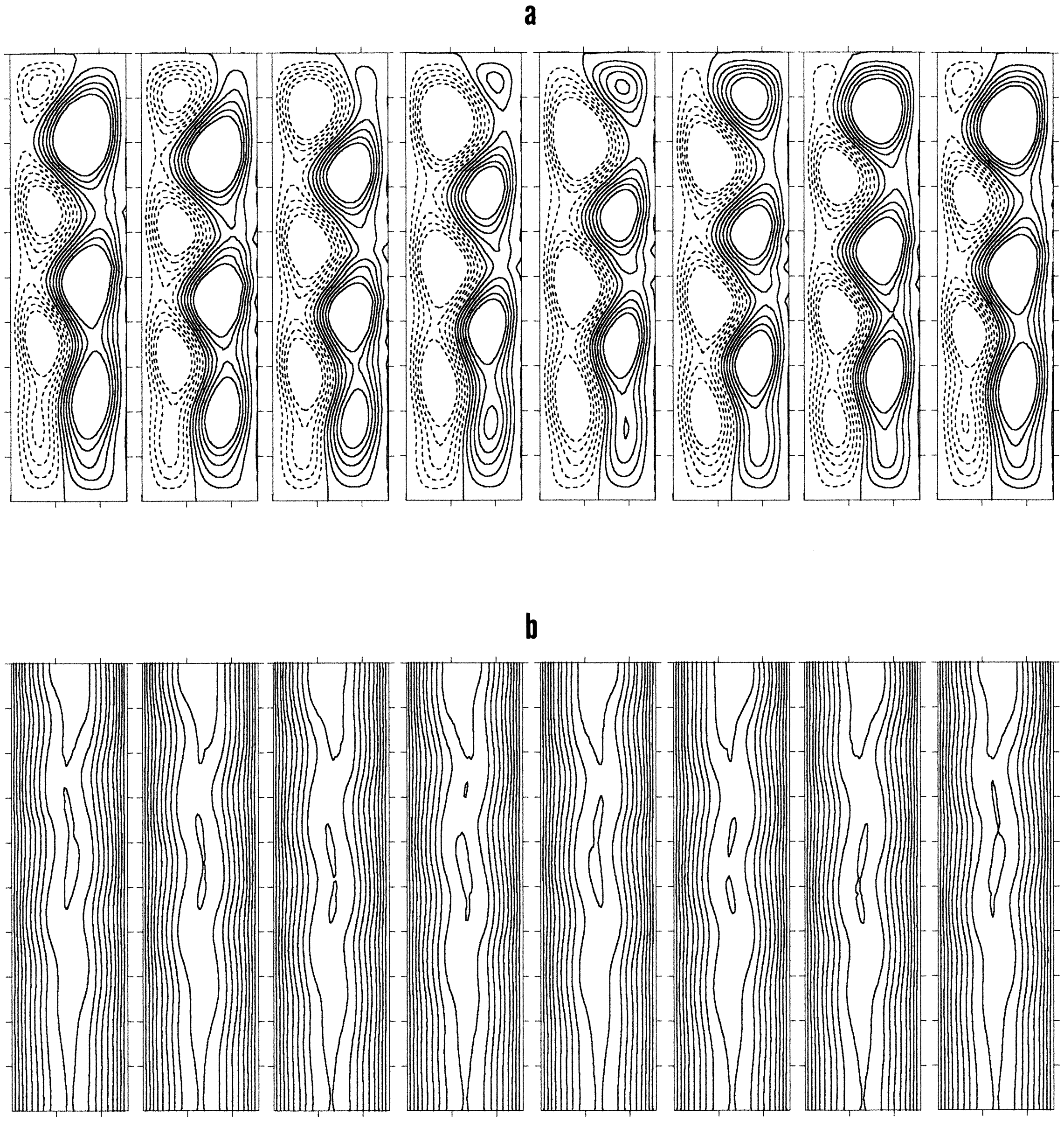

Fig. 8. Snapshots of flow and temperature fields for $Gr = 3.79 \times 10^5$ after periodic flow has been attained. Dimensionless time interval between frames ~0.63. The sequence covers approximately one period. (a) Streamlines, dimensionless separation = 0.2. Solid lines: clockwise flow; broken lines: anti-clockwise flow. (b) Isotherms, dimensionless separation = 0.1.

cous dissipation once they approach the bottom wall. The period t_P after which the flow field repeats itself identically (renewal time of the roll pattern) is ~4.7 in dimensionless terms and corresponds to the time necessary for a pair of rolls (clockwise/anticlockwise) to be formed. Note that the lifetime of a single roll is about $3t_P$ since three pairs of rolls (in the average) are present in the cavity. The left and right halves of the cavity experience the same states within a given period, but with a time lag of half a period as observed by discussing the time behaviour of various quantities at symmetric monitoring points.

Examples of velocity and temperature power spectra at monitoring point P_1 are represented in Fig. 9. Spectra were normalized so that their integral was 1. They exhibit markedly separate individual lines correspond-

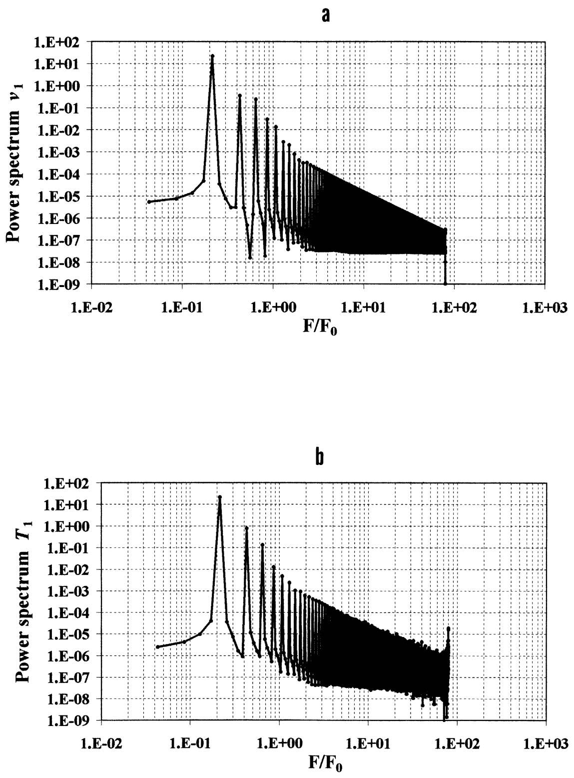

Fig. 9. Normalized power spectra of vertical velocity (a) and temperature (b) at monitoring point 1 for $Gr = 3.79 \times 10^5$ (periodic flow).

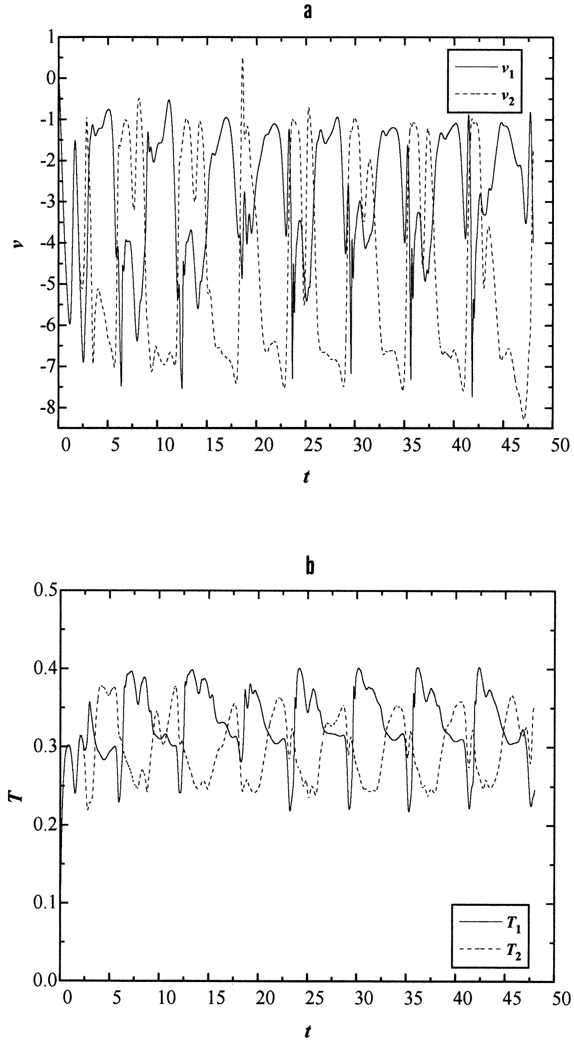

Fig. 10. Behaviour of vertical velocity v (a) and temperature T (b) at monitoring points 1 and 2 for $Gr = 1.26 \times 10^6$.

ing to discrete frequencies, in accordance with the periodic nature of the flow. The highest peak occurs at the main periodic frequency f_P, while all secondary maxima correspond to its higher harmonics, related to the shape of the original signal. The highest frequency still having a significant energy content (say, $\geq 10^{-3}$ times the main peak) is $\sim 5f_P$ for both, velocity and temperature.

7. Transition to chaotic behaviour

The periodic regime exists only in a narrow range of Grashof numbers; as Gr increases above $\sim 10^6$, the perfect periodicity behaviour is replaced by an irregular behaviour. This is illustrated in Fig. 10, where, for $Gr = 1.26 \times 10^6$, velocities (a) and temperatures (b) are shown at monitoring points 1 and 2 as functions of t during the whole simulation time ($\sim$48). The approximate periodicity is quite evident, but many irregularities are present. Unlike in the periodic cases, curves relative to points which are symmetrical in space are not identical and shifted in time, but rather exhibit a completely different shape. The main period which can be identified in the figure still corresponds to the roll renewal time and is $t_P \approx 5.8$ ($f_P \approx 0.17$), close to that ($\sim$0.15) observed in the periodic case at $Gr = 7.03 \times 10^5$. On the basis of the relatively short simulation time, it is difficult to ascertain whether the flow at this Grashof number is properly chaotic or rather quasi-periodic (i.e., possessing two incommensurate frequencies and their harmonics, and characterized by an open orbit confined on a torus). Quasi-periodic regimes between periodic and chaotic flow have been identified in *differentially heated* cavities [27].

Fig. 11 shows time sequences of instantaneous flow and temperature fields, well after the initial transient has died away. Separation between frames is 0.57 time

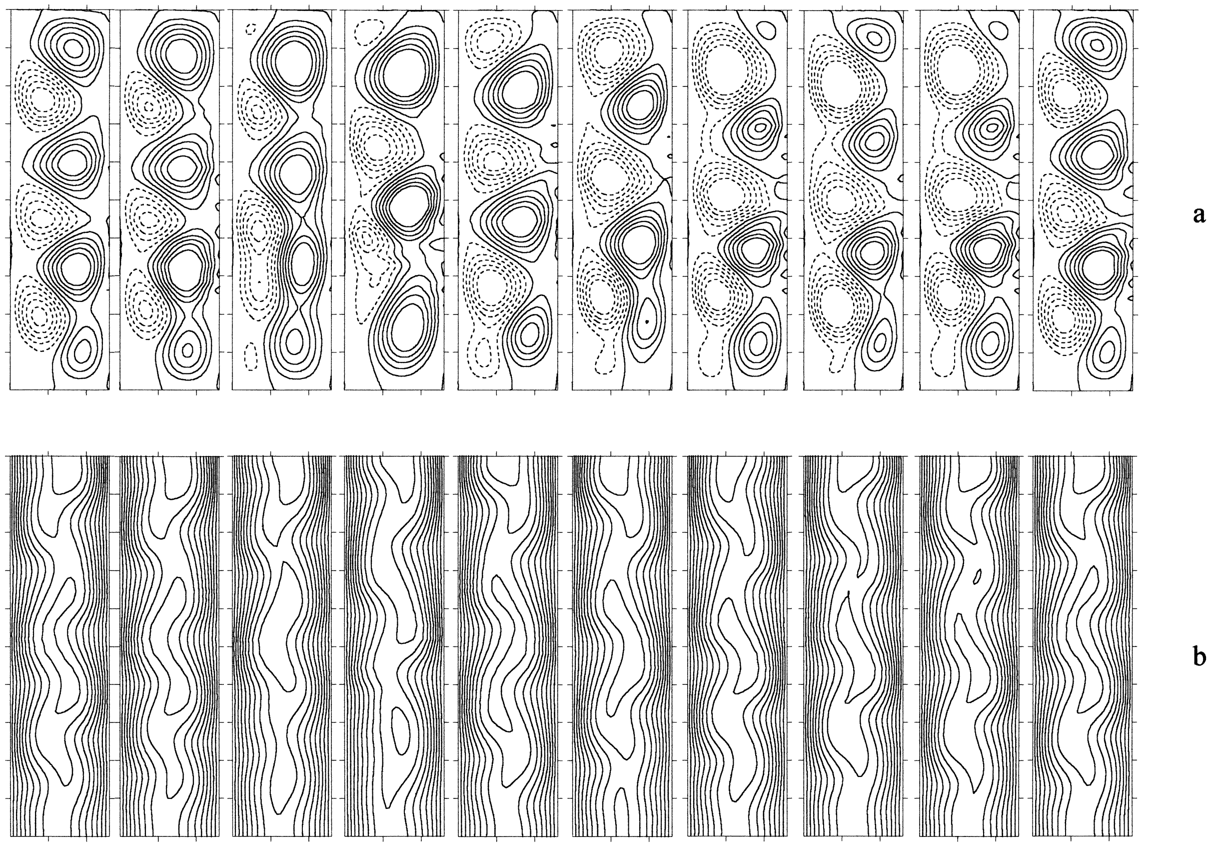

Fig. 11. Sequence of flow field and temperature distribution for $Gr = 1.26 \times 10^6$ after an almost periodic flow has been attained. Dimensionless time interval between plots ~0.57. The sequence covers approximately one period t_P. (a) Streamlines, dimensionless separation = 0.2. Solid lines: clockwise flow; broken lines: anti-clockwise flow. (b) Isotherms, dimensionless separation = 0.1.

units; thus, the sequence shown extends approximately over one main period t_P. Rolls are alternately generated in the top corners as in the periodic case of Fig. 8; now, however, they move downwards regularly only until they reach approximately the mid height of the cavity, while, in the lower part of the descent, irregular and abrupt coalescence events occur. The coalescence of rolls seems to be an important mechanism of roll destruction and mechanical energy dissipation, besides the simple viscous damping which was the only mechanism acting in the periodic case. As in the previous, periodic-flow cases, the temperature distribution is much smoother than the streamline distribution, due to the dominating role played by conduction in a low Prandtl number fluid.

8. Fully chaotic flow

When the Grashof number is made to increase above $\sim 2 \times 10^6$, the flow becomes completely chaotic. Four different Grashof numbers were investigated in this range: 3.79×10^6, 3.79×10^7, 3.79×10^8, and 1.26×10^9.

Fig. 12 shows maximum and average temperatures of the fluid as functions of time for the four cases. Note that the dimensionless duration of the initial transient increases with Gr for the reasons discussed in Section 5. The amplitude of the overshoot following the initial rise in the maximum or average temperature decreases with increasing Gr due to increased mixing; no overshoot is recognizable in $\langle T \rangle$ for the two highest Grashof numbers, i.e. $Gr \approx 3.79 \times 10^8$ and 1.26×10^9. For the same reason, the most intense time fluctuations in $\langle T \rangle$ or $T_{\max}$ are observed at the lowest values of Gr ($Gr \approx 3.79 \times 10^6$ and 3.79×10^7).

Fig. 13 reports consecutive "snapshots" of stream function (a) and temperature (b) in the startup phase (up to $t \approx 4.4$) for $Gr = 3.79 \times 10^8$. The separation between frames is 0.55 time units. The stream function evolution (a) shows that, in the first instants, a single large natural convection cell appears on each side of

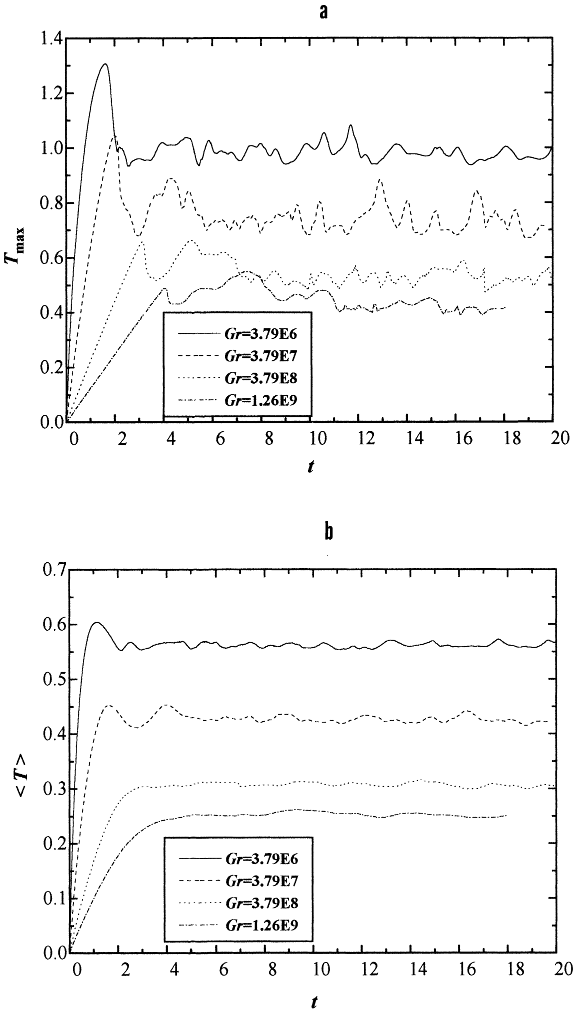

Fig. 12. Behaviour of maximum (a) and average (b) temperatures as function of time for four fully-chaotic cases.

the cavity, with a stronger circulation in the bottom region (by contrast, the initial stronger circulation was located in the top half of the cavity in the periodic case $Gr = 3.79 \times 10^5$, see Fig. 7a). At $t \approx 2.2$ (frames 4–5), two shear-induced counter-rotating vortices start to grow in the bottom corners while the previous main convection cells move upwards. Up to this instant, the spatial symmetry with respect to the vertical midline is still preserved.

In the later instants, as the main circulation cells rise, regions of low-speed fluid appear between these structures and the counter rotating vortices (frame 6, $t \approx 3.3$). At this point the left–right symmetry is broken and the fluid motion becomes chaotic. The initial symmetry breaking occurs as the inwards-directed horizontal jets resulting from the detached wall boundary layers (and initially impinging symmetrically on the cavity midline) abruptly overtake each other and interpenetrate (frames 6–7). This instability is peculiar to the high Grashof number cases and was totally absent in the periodic case, Fig. 7(a). However, the instability mechanism (lateral oscillation of the rising plume) described for the periodic case is still present.

The corresponding temperature sequence is illustrated in Fig. 13b. The initial growth of a horizontal thermal stratification and the penetration of cold fluid into the bottom central region characterize the early stages of the transient (frames 1–3). However, the horizontal stratification is progressively accompanied by a significant vertical stratification (frames 3–5). The difference with the periodic case in Fig. 7b, in which the vertical stratification was negligible, can be observed. Animations of streamlines or isotherms clearly show travelling-wave disturbances which propagate downwards along the edges of the vertical boundary layers.

The shear-induced counter-rotating vortices which are formed at the bottom corners of the cavity (frames 4–6 in the streamline sequence) determine corresponding regions of unstable thermal stratification in the bottom part of the cavity, which also contribute to chaotic mixing (frame 6 and following). In the same frames, further smaller regions of unstable thermal stratification can be observed also in the top region of the cavity. All instability mechanisms seem to occur almost simultaneously at $t \approx 3.3$ (frame 6).

Following the interval shown in Fig. 13, the further evolution of the flow and thermal fields is fully chaotic. Fig. 14 shows the behaviour of the vertical velocity as a function of time in the monitoring points 1 (a) and 4 (b) of Fig. 1 for the same chaotic cases. For clarity purposes, only sequences of duration ~6 (dimensionless) have been reported, all well after the initial transient has died away. In the whole range of Grashof numbers considered, several frequencies appear clearly in the time series. The higher frequencies are observed only for part of the time (e.g. $t \approx 12$–13 for the velocity v_1 relative to $Gr \approx 1.26 \times 10^9$), giving rise to a typical *intermittent* behaviour. Intermittence seems to be associated with the rapid coalescence of two rolls as observed in sequences of the flow field and is more evident in the bottom region of the cavity (monitoring point 1).

Fig. 15 reports the temperature as a function of time at the same monitoring points 1 (a) and 4 (b) for the different cases. High frequencies are still present at point 1, located in the lower left region of the cavity, but are almost completely absent at point 4, located near the cavity midline and within the upper region of the rising plume.

Power spectra of vertical velocity v (a) and temperature T (b) are presented in Fig. 16 for $Gr = 1.26 \times 10^9$

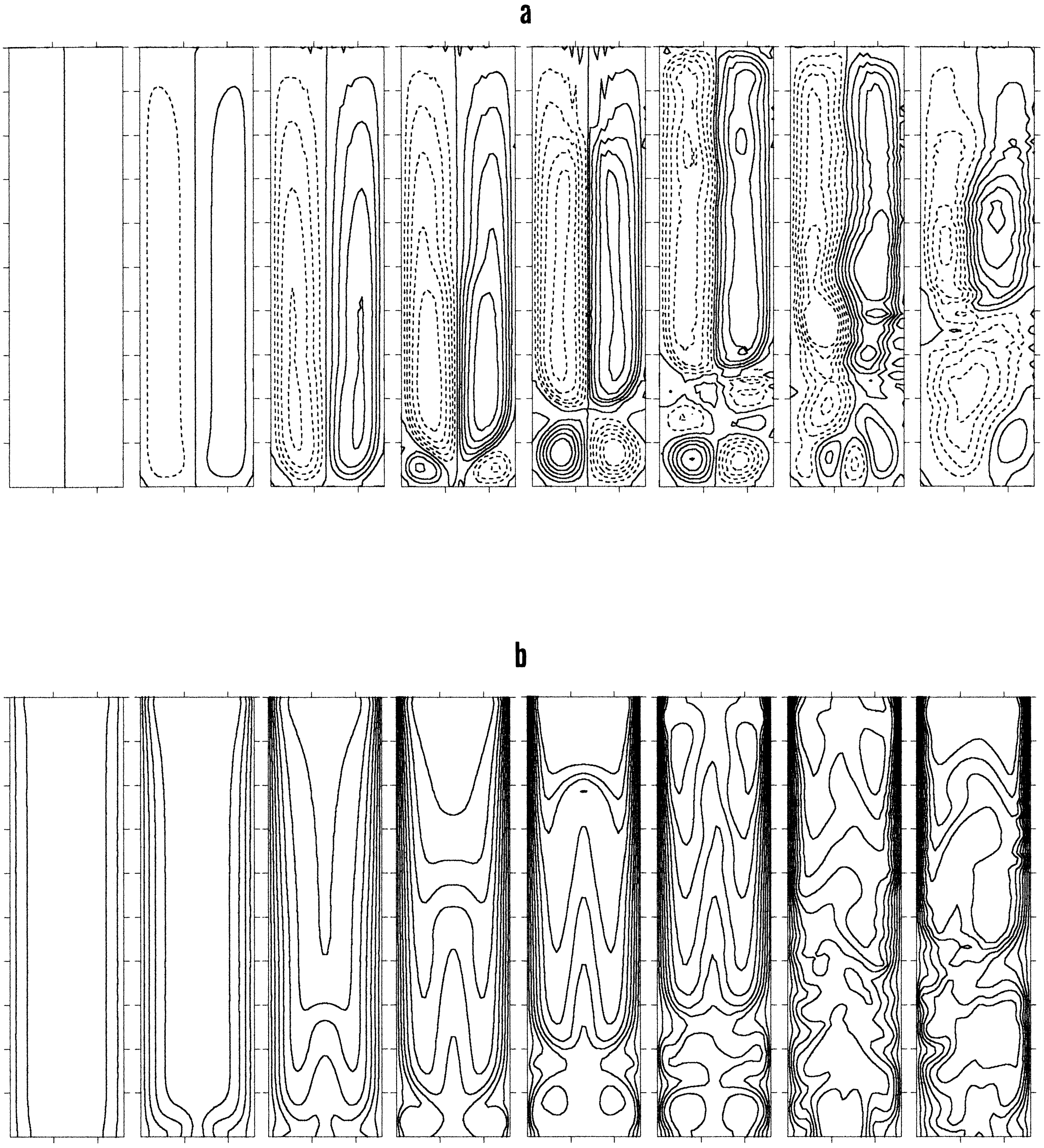

Fig. 13. Initial transient for $Gr = 3.79 \times 10^8$ (chaotic flow). Dimensionless time interval between frames ~0.55. (a) Streamlines, dimensionless separation = 0.2. Solid lines: clockwise flow; broken lines: anti-clockwise flow. (b) Isotherms, dimensionless separation = 0.05.

at monitoring point 1. Four regions can be clearly identified in the spectra:

1. Low-frequency region ($f \leq 1$): here, particularly in the velocity spectrum, Fig. 16a, the main features are broad peaks corresponding to the roll renewal frequency f_P (≈ 0.3 for the present case) and to its first harmonic at $2f_P$ (≈ 0.6). Peaks are broadened, unlike in the periodic spectra illustrated in Fig. 9, due to chaotic frequency modulation.
2. Intermediate, energy-containing, region ($1 \leq f \leq 10$).

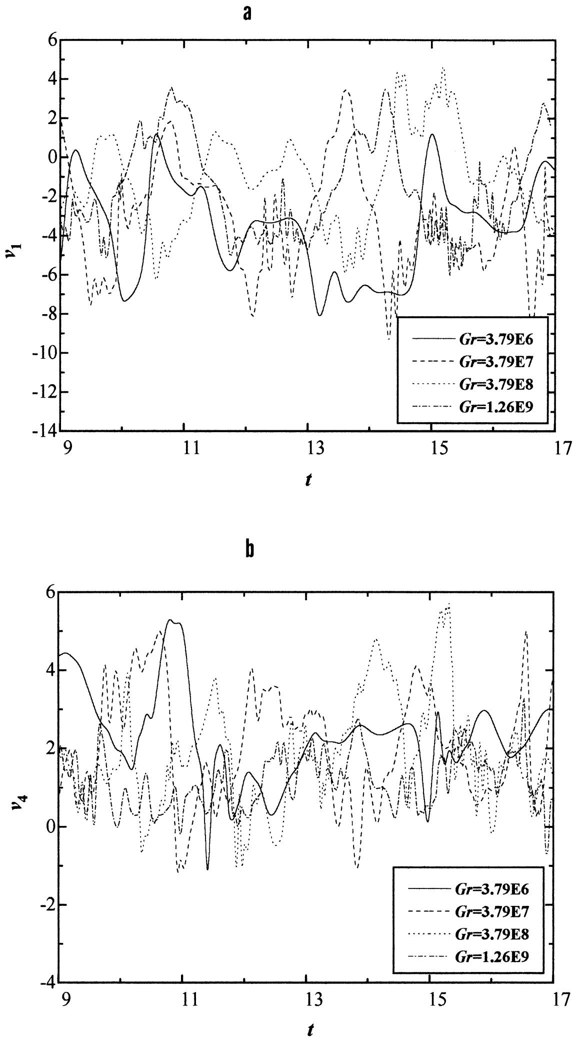

Fig. 14. Behaviour of vertical velocity v at two monitoring points for four chaotic cases. (a) Point 1 (lower left region of the cavity). (b) Point 4 (close to cavity midline in the upper region).

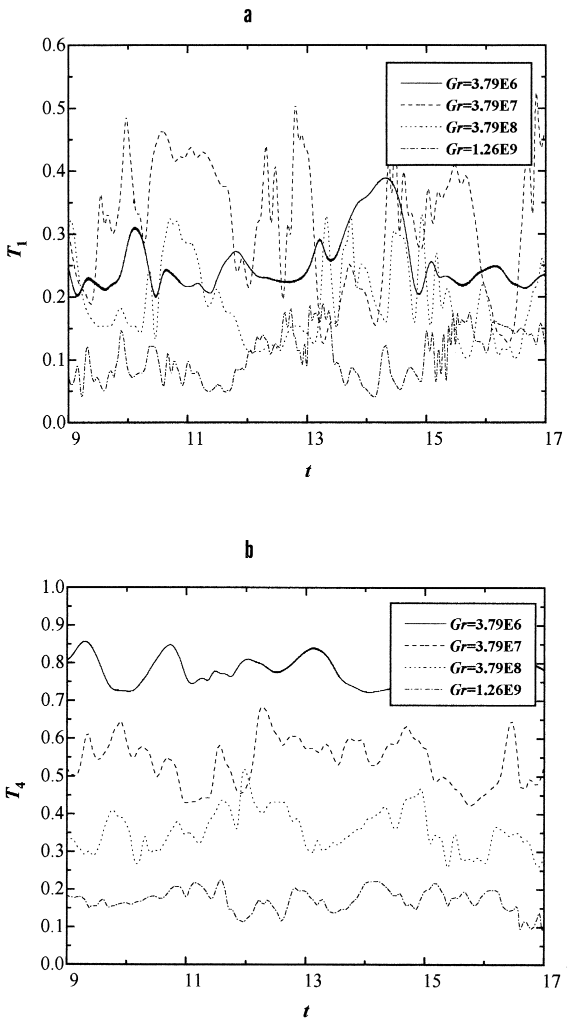

Fig. 15. Behaviour of temperature T at two monitoring points for four chaotic cases. (a) Point 1 (lower left region of the cavity). (b) Point 4 (close to cavity midline in the upper region).

This region corresponds to chaotic structures still having a significant power content and is characterised by a slope (indicated in Fig. 16) close to $-5/3$, i.e. to the theoretical value expected for the inertial Kolmogorov sub-range of spectra for homogeneous isotropic turbulence [26].

3. Dissipation region ($10 \le f \le 30$–50). This region is characterized by a steep fall of the power content of the fluctuations, with a slope of ~ -6 for v and -9 for T. The (dimensionless) cutoff frequency of ~ 10 can be identified with the Kolmogorov frequency f_K of the dissipative eddies, and is much lower than the highly conservative value (~ 400) which can be deduced from the a priori criteria described in Section 4. By applying Taylor's hypothesis of "frozen turbulence" and keeping the definitions of vortex renewal frequency f_P and dissipative frequency f_K in mind, a simple analysis shows that the dimensionless wavelength λ_K of the dissipative eddies can be expressed as:

$$\lambda_K = \frac{AR}{N} \cdot \frac{f_P}{f_K} \tag{15}$$

where N is the number of *pairs* of recirculation rolls (one clockwise, one anti-clockwise) along the height of the cavity. For the case $Gr \approx 1.26 \times 10^9$ in Fig. 16, one has $N \approx 3$, $f_P \approx 0.3$ and $f_K \approx 10$ (dimensionless values), so that Eq. (15) yields $\lambda_K \approx 0.036$, which is

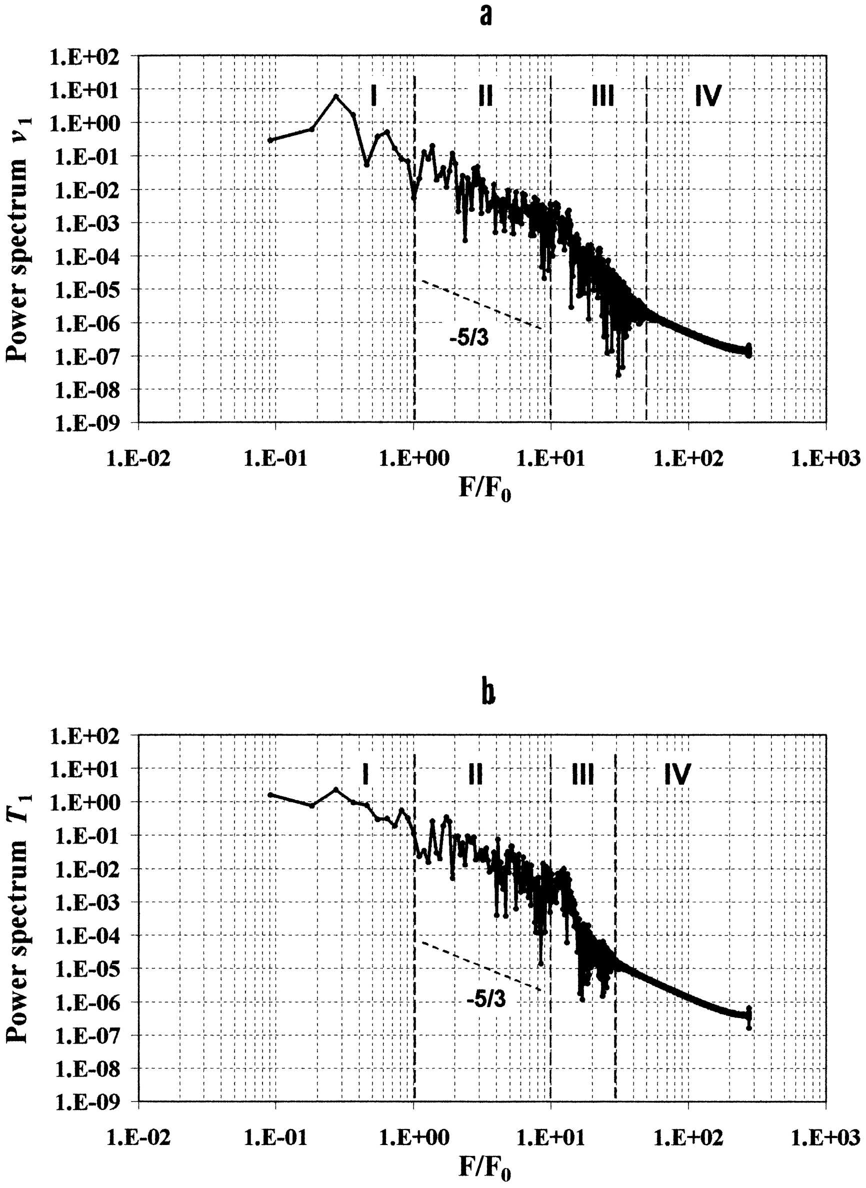

Fig. 16. Normalized power spectra of vertical velocity (a) and temperature (b) at monitoring point 1 for $Gr = 1.26 \times 10^9$ (chaotic flow).

much larger than the average size of the computational mesh used (128 × 220 nodes). This suggests that all significant scales are actually resolved by the simulation. Similar spectra for point 4 (cavity midline) exhibit similar features but a lower cutoff frequency ($f \approx 3$–5).

4. Numerical $1/f$ "tail" between $f \approx 30$–50 and $f = f_{\max} = 1/(2\delta t) \approx 280$, inevitably associated with the numerical implementation of the FFT algorithm and devoid of physical meaning.

Fig. 17 reports consecutive instantaneous snapshots of stream function (a) and temperature (b) similar to those shown for the startup phase in Fig. 14, but well after the initial transient has died away. The frames cover roughly 2.8 time units at dimensionless intervals of ~0.4. The flow evolves with continuous birth, descent, coalescence and disruption of large coherent structures (rolls). Animation of the streamlines show a "gearbox"-like motion, with moving cogwheels having non-stiff boundaries. The dominating energy dissipa-

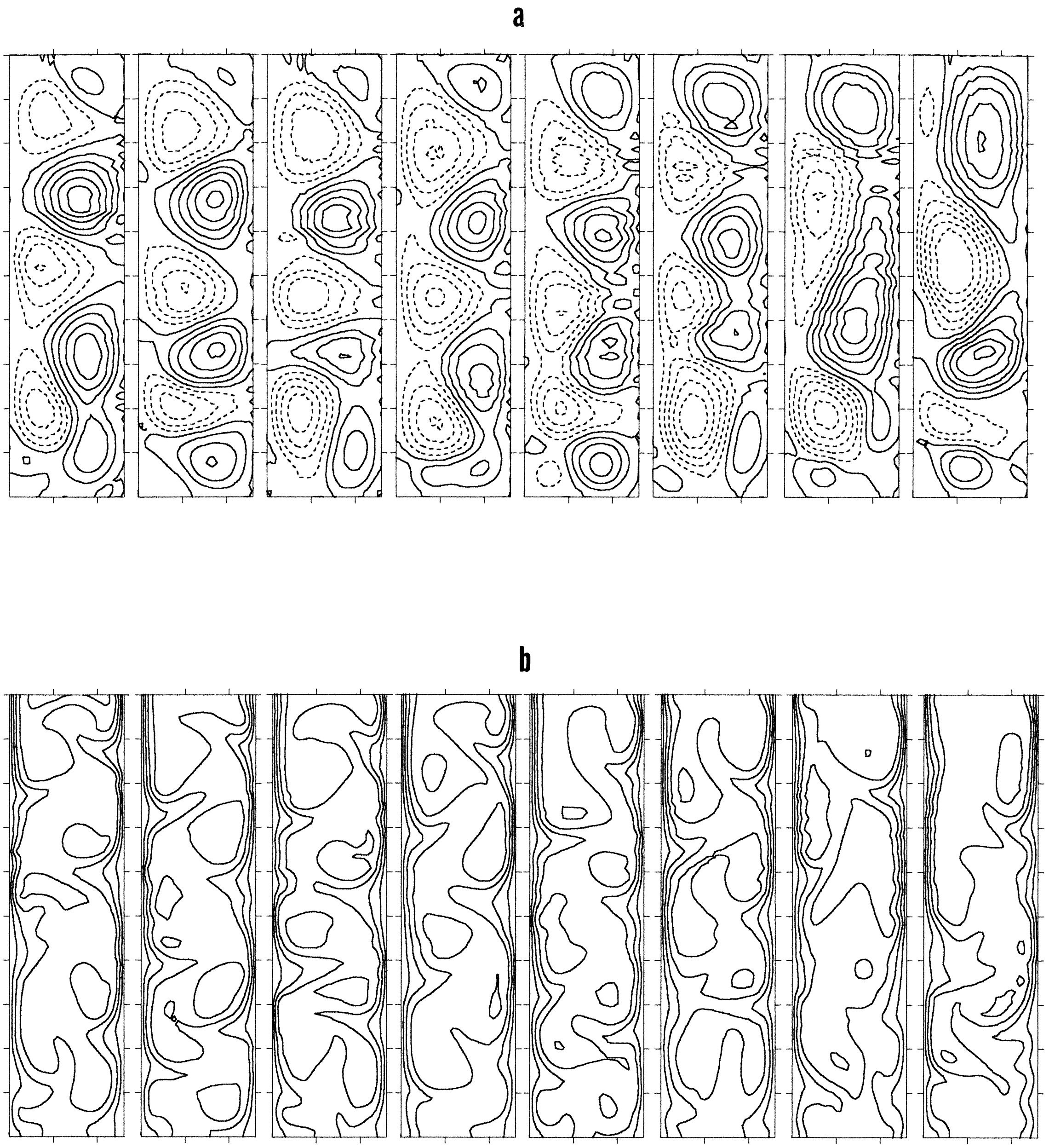

Fig. 17. Snapshots of flow and temperature fields for $Gr = 3.79 \times 10^8$ (chaotic flow) after the initial transient has died away. Dimensionless time between frames ~0.4. (a) Streamlines, dimensionless separation = 0.2. Solid lines: clockwise flow; broken lines: anti-clockwise flow. (b) Isotherms, dimensionless separation = 0.1.

tion mechanism seems to be the coalescence of co-rotating rolls (e.g frames 4–7). The evolution of the temperature field, shown in Fig. 17b, shows that, at any instant, several regions of unstable thermal stratification are scattered throughout the cavity, with hot spots corresponding to the centres of the convective rolls where minimum mixing occurs.

9. Roll renewal frequency

As discussed previously, in all cases of unsteady (either periodic or chaotic) flow, the time dependence is dominated by the roll renewal frequency f_P. For each test case, the most reliable way to estimate this periodic frequency is the direct examination of

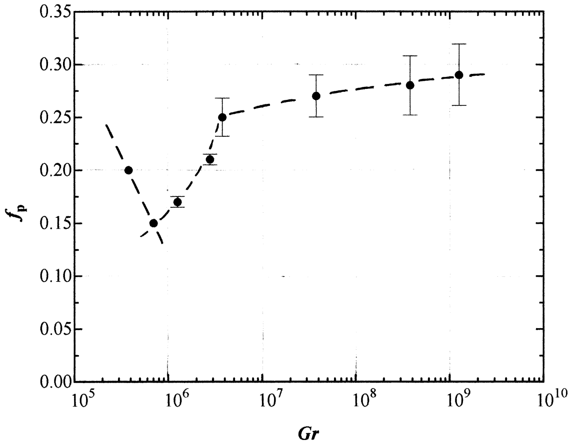

Fig. 18. Roll renewal frequency f_P as a function of the Grashof number for all the unsteady-flow cases simulated. Uncertainty bars are shown (see text). Qualitative trend lines were added for clarity purposes.

sequences of streamline maps: the time $t_P = f_P^{-1}$ can be identified with the interval by which consecutive pairs of recirculation rolls appear in the upper region of the domain.

Results are summarized for all unsteady cases in Fig. 18, in which f_P is reported as a function of the Grashof number. Uncertainty bars indicate the range of oscillation of f_P during the simulation time; of course, the initial transient was excluded from the estimate. Qualitative trend lines were added for clarity purposes.

Note that f_P is normalized by the reference frequency $F_0 = (g\beta\vartheta_c/D)^{1/2}/(2\pi)$, i.e. actually a Strouhal number. In this form, it decreases slightly with Gr in the narrow periodic-flow range, presents a minimum of $\sim$0.15 for $Gr \approx 7.03 \times 10^5$ and then increases as $Gr^{1/3}$ through the quasi-periodic and early chaotic range, attaining a value of $\sim$0.25 at $Gr = 3.79 \times 10^6$. The further increase of Gr from 3.79×10^6 to 1.26×10^9 (fully chaotic range) leads only to a small increase of f_P, from $\sim$0.25 to $\sim$0.30.

On the whole, the variation of f_P over a very broad range of Grashof numbers (covering $3\frac{1}{2}$ decades) is very small, which indicates that the $Gr^{1/2}$ dependence included in f_0 accounts for most of the Grashof number effects. The same conclusion was reached, for example, by Henkes and Hoogendoorn [27] in their simulations of differentially heated cavity flow. The roll renewal frequency computed here for the case of periodic flow (0.15–0.20) is close to that obtained by Janssen and Henkes [28] for a differentially heated square cavity at $Pr = 0.71$ (0.12 in the present units), despite the large difference in the problem's conditions. It is also of the same order as that computed by May [17] for a square enclosure with internal heat generation and four isothermal walls at $Pr = 7$ (0.05 in the present units). This supports the universality of the frequency scale adopted here and, in particular, the choice of the cavity width D (rather than its height H) as the fundamental length scale.

In order to illustrate the kind of thermal stratification which is established in the cavity at different Grashof numbers, Fig. 19 reports vertical profiles of the horizontally- and time-averaged temperature:

$$\langle \bar{T} \rangle_x(y) = \int_{-1/2}^{1/2} \bar{T}(x, y)\,\mathrm{d}x \tag{16}$$

Results from steady-state, periodic, and chaotic-flow cases have been included in this figure. It can be observed that, through the low-Gr, steady-state cases and the first periodic case ($Gr = 3.79 \times 10^5$), the vertical stratification is very low due to the marginal role of convection as compared to conduction. All cases from $Gr = 7.03 \times 10^5$ to 3.79×10^6 (including periodic, quasi-periodic and chaotic flow) present an inversion in the vertical $\langle \bar{T} \rangle_x$ profile, with unstable thermal stratification (in the time and x-averages) between $y \approx 0$ and 1. As Gr increases further, this inversion disappears due to increasing mixing and the $\langle \bar{T} \rangle_x$ profile reverts to the monotonic behaviour typical of low-Gr cases, but with a larger excursion between bottom and top. In the whole range of the unsteady flow cases, vertical stratification varies very little; as Gr increases, the decrease in the temperature close to the top wall (due to increased mixing) is compensated by a comparable reduction of the temperature close to the bottom wall (due to a more effective penetration of the downcoming boundary layers as they leave the cold wall and turn towards the cavity midline). As a consequence, the profiles of $\langle \bar{T} \rangle_x$ in Fig. 19 shift downwards but their slope remains roughly unaltered. If this slope is computed as:

$$C = \langle \bar{T} \rangle_x(y = +AR/2) - \langle \bar{T} \rangle_x(y = -AR/2) \tag{17}$$

then it remains close to 0.25 over the whole unsteady Grashof number range.

10. Dynamics and time averages

The overall dynamics of the flow and temperature fields is illustrated for different values of the Grashof number in Fig. 20. Here, the values of the vertical velocity v at the two monitoring points 1 and 2 of Fig. 1 (which are symmetrically located with respect to the cavity midline) are plotted against each other during the dynamic evolution of the flow after the initial transient has ended. The graphs are all for the same

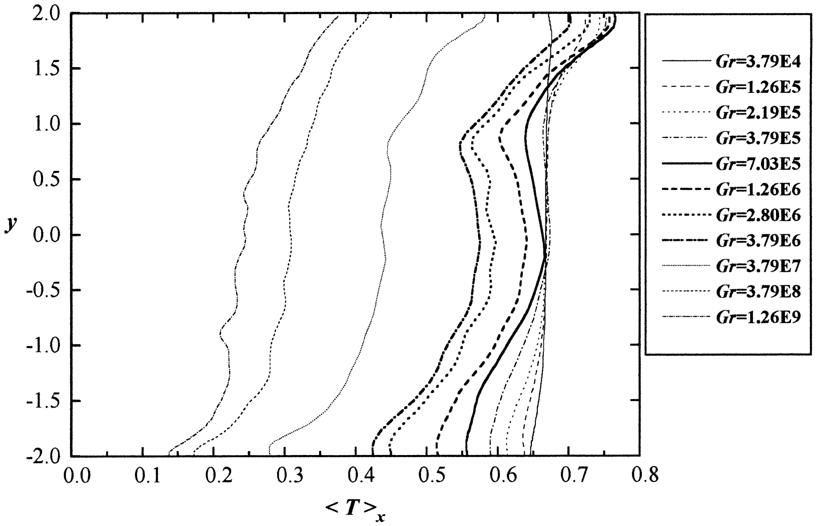

Fig. 19. Vertical profiles of the time- and horizontally-averaged temperature $\langle\bar{T}\rangle_x$ for all the test cases simulated, showing thermal stratification.

dimensionless duration (~20), thus encompassing from 3 to 6 main periods t_P.

In all cases, during the initial transient (not reported in the figure for the sake of readability), the point (v_1, v_2) starts from the origin (initial conditions of zero velocity everywhere), moves along the bisecting line $v_1 = v_2$, departs from it when the left–right symmetry is broken, and eventually enters an asymptotic orbit. Thus, each of the plots in Fig. 20 can be regarded as the projection of a finite region of the system's attractor (which is embedded in the multi-dimensional phase space of the system's degrees of freedom) onto the plane (v_1, v_2). For simplicity, we will call it *the attractor* in the following.

Of course, in the steady-state flow cases (not reported), in which spatial symmetry is preserved, the representative point never leaves the bisecting line $v_1 = v_2$, and the attractor collapses to a single point lying on the same line.

In the periodic cases like that at $Gr = 3.78 \times 10^5$, graph (a), the attractor is an eight-shaped limit cycle which is swept repeatedly during the simulation. Thus, a Hopf bifurcation occurs between $Gr = 2.19 \times 10^5$ (highest value for which a steady-state solution was obtained) and $Gr = 3.78 \times 10^5$. The period of the eight-shaped orbit coincides with the previously discussed roll renewal time $t_P = f_P^{-1}$. The attractor itself is perfectly symmetric with respect to the bisecting line $v_1 = v_2$, which causes the characteristic flow behaviour discussed in Section 6 and makes long-term averages perfectly symmetric with respect to the cavity midline $x = 0$, see following Fig. 21.

The following case $Gr = 1.26 \times 10^6$, graph (b), is slightly beyond the breakdown of perfect periodicity, as shown also by the time sequences previously reported in Figs. 10 and 11. The trajectory in the (v_1, v_2) plane now describes consecutive orbits which are only roughly similar to one another. Moreover, each orbit does not exhibit left–right symmetry.

Graphs (c) and (d) in Fig. 20 refer to Grashof numbers in the chaotic range. The increasing entanglement of the trajectories can be observed. The symmetry of the attractor with respect to the bisecting line $v_1 = v_2$, however, does *not* vary monotonically with *Gr*, but rather seems to increase again as compared with the strongly asymmetric case $Gr = 1.26 \times 10^6$ in graph (b). Moreover, the region of the phase space occupied by the trajectories tends to shrink and become more regular as *Gr* increases.

For some of the test cases simulated, the following Figs. 21 and 22 report time averages and statistics relative to an integral number of main periods t_P (6–8).

Fig. 21 shows the time-averaged stream function. In the periodic case $Gr = 3.79 \times 10^5$ (a), consistently with the attractor's behaviour illustrated in Fig. 20(a), the time-averaged flow field exhibits a perfectly left–right symmetric configuration, with a single recirculation cell on each side. The circulation centres are shifted towards the bottom of the cavity. In the following case $Gr = 1.26 \times 10^6$ (b), the time-averaged flow field is markedly asymmetric, which, too, is consistent with the asymmetric shape of the attractor in Fig. 20(b). Moreover, the circulation exhibits a multi-cellular pattern. Finally, as *Gr* increases, e.g. to 3.79×10^8 (c), the symmetric and uni-cellular circulation pattern is partly recovered.

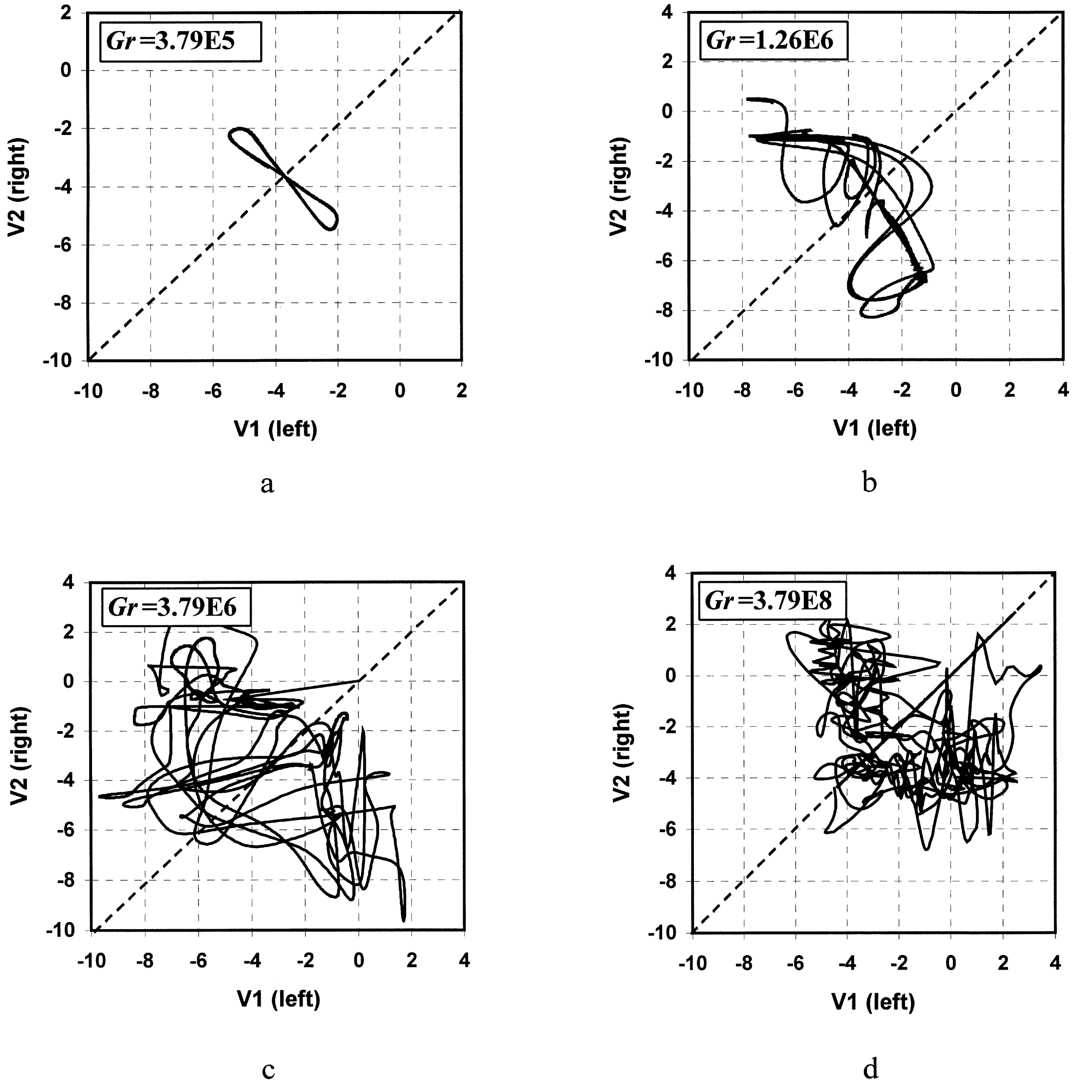

Fig. 20. Plots of vertical velocity at point 2 versus vertical velocity at point 1 for four test cases during ~20 time units. (a) $Gr = 3.79 \times 10^5$; (b) $Gr = 1.26 \times 10^6$; (c) $Gr = 3.79 \times 10^6$; (d) $Gr = 3.79 \times 10^8$.

The time-averaged temperature field is shown for the same test cases in Fig. 22. As *Gr* increases, the central region which presents a significant thermal stratification spreads, while the vertical thermal boundary layers become thinner. The same remarks as above hold as far as the symmetry of the time-averaged solution is concerned.

A careful analysis of time sequences shows that the above illustrated symmetry properties of trajectories and time averages depend crucially on the size of the circulation rolls and thus on the exact number of them that can simultaneously occupy the cavity volume at any instant. As shown by Fig. 8a, in the periodic case $Gr = 3.79 \times 10^5$ the cavity is filled during most of the time by three rolls on each side, arranged in a staggered configuration. This should be compared with Fig. 11a, in which a time sequence covering approximately one main period t_P (~5.8) was reported for the case $Gr = 1.26 \times 10^6$. It can be observed that the mean size of recirculation rolls is smaller than in the previous case, so that the cavity accommodates for most of the time *four* rolls on one side (the right one in the present realization) but only *three* on the opposite side (left in the present realization). This causes trajectories in Fig. 20b, as well as time averages in Fig. 21b, to be markedly asymmetric. As *Gr* increases, the mean size of rolls increases again so that for $Gr = 3.79 \times 10^8$, as shown in Fig. 17, three rolls per side are again present

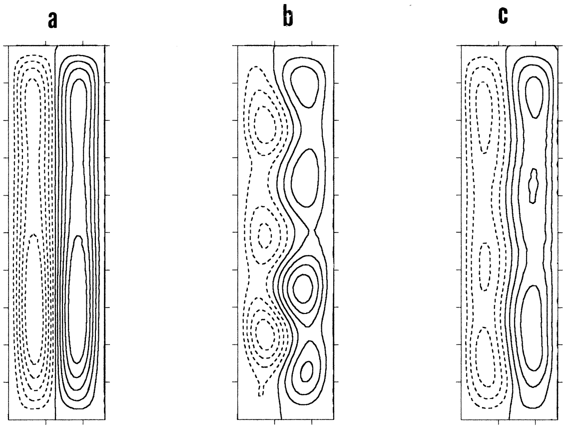

Fig. 21. Time-averaged streamlines (dimensionless interval = 0.2). (a) $Gr = 3.79 \times 10^5$; (b) $Gr = 1.26 \times 10^6$; (c) $Gr = 3.79 \times 10^8$.

during most of the time, giving the more symmetric behaviour in Fig. 21c.

11. Shear stress and heat transfer

Fig. 23(a) reports time-averaged profiles of the wall shear stress along the side walls for all the cases studied. The wall shear stress was further averaged between the left and right walls and normalized by ρU_0^2, thus taking the form of a friction coefficient C_f.

All curves exhibit a peak near the cavity top, where the horizontal boundary layers turn and meet the cold walls; in periodic and transitional cases, this is followed by a gradual increase towards the cavity bottom, associated with the increasing fluctuation intensity in the downcoming boundary layers, while, in fully chaotic cases, the overall profile is much flatter over most of the wall length.

Fig. 23(b) reports the spatially-averaged value of C_f as a function of Gr over the whole range studied. At the lowest values of Gr, the computed values of C_f are very close to the value $4\pi^2/15 \approx 2.63$ deduced from the analytical solution discussed in Section 3, which can be regarded as the asymptotic limit of C_f for $Gr \rightarrow 0$. At higher Gr, C_f scales roughly as $Gr^{-1/3}$, i.e. the *dimensional* wall shear stress scales as $U_0^{4/3}$, thus exhibiting a behaviour intermediate between that of a viscous and a hydraulic resistance.

For the present configuration, the mean value of the wall heat flux under thermal equilibrium conditions is $qD/2$; this value can be used to normalize the local and/or instantaneous values of the wall heat flux q''. Fig. 24a reports the wall heat flux profiles for all the cases studied; all curves represent long-term time

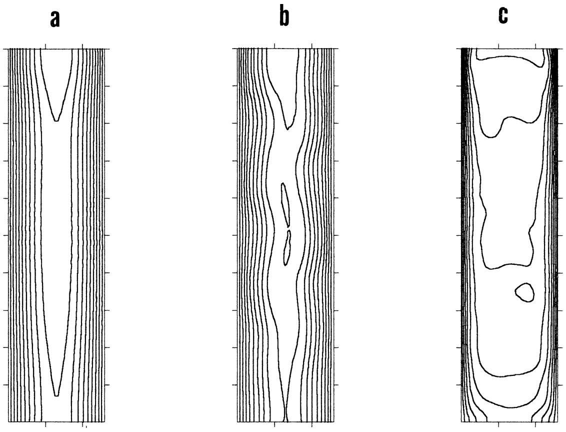

Fig. 22. Time-averaged isotherms (dimensionless interval = 0.1). (a) $Gr = 3.79 \times 10^5$; (b) $Gr = 1.26 \times 10^6$; (c) $Gr = 3.79 \times 10^8$.

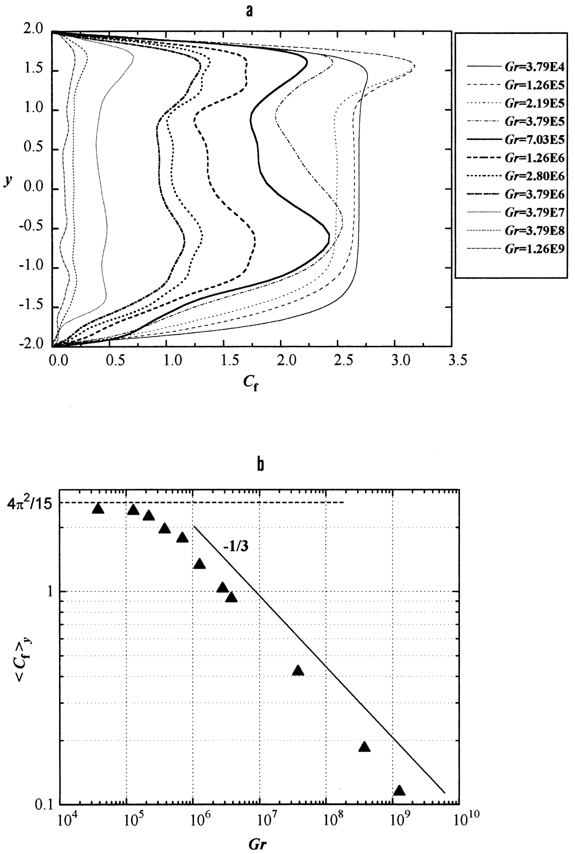

Fig. 23. Time-averaged friction coefficient C_f. (a) Profiles along the vertical walls for all cases investigated. The mean of left and right wall values is shown. (b) Dependence of the spatially-averaged value $\langle \bar{C}_f \rangle_y$ upon the Grashof number.

averages which were further averaged between the left and right walls and plotted against the non-dimensional vertical co-ordinate.

For the steady-state and periodic cases the curves are rather flat, with small variations with respect to the mean value. On the other hand, large variations are present for higher Grashof numbers in the chaotic range. Peak values are obtained in correspondance with the impingement of hot fluid on the cold walls near the cavity top, while lowest values correspond to the separation of the wall boundary layers near the cavity bottom. A flat distribution of q'' is obtained in the central region of the cavity.

The influence of Gr on heat transfer is better shown in Fig. 24b. This reports the quantities $Nu_1 = 1/T_{\max}$ ($T_{\max}$ being the time-averaged maximum temperature in the cavity) and $Nu_2 = (2/3)/\langle T \rangle$ ($\langle T \rangle$ being the time- and space-averaged temperature). This latter definition is such that it gives $Nu_2 = 1$ for a purely conductive temperature distribution. Both quantities can be regarded as alternative definitions of the Nusselt number (ratio of overall to conductive heat transfer) for the present configuration; they are plotted as functions of the Grashof number, showing results from all cases examined. It is interesting to observe that, for Grashof numbers below 2×10^6 (steady-state, periodic and transitional conditions), convection actually results in an *increase* of the temperature maximum ($Nu_1 < 1$) by transporting hot fluid into the hottest region of the enclosure (adjacent to the top adiabatic wall). A similar minimum $Nu_1 < 1$ in correspondence with transitional values of Gr for internally heated cavities was observed by De Socio et al. [29].

As expected in liquid metals, Nu_1 and Nu_2 never attain very high values, being ~2.4 and ~2.7, respectively, at the highest Gr studied (1.26×10^9). This shows that even the energetic turbulent convection prevailing at high Gr enhances heat transfer only moderately.

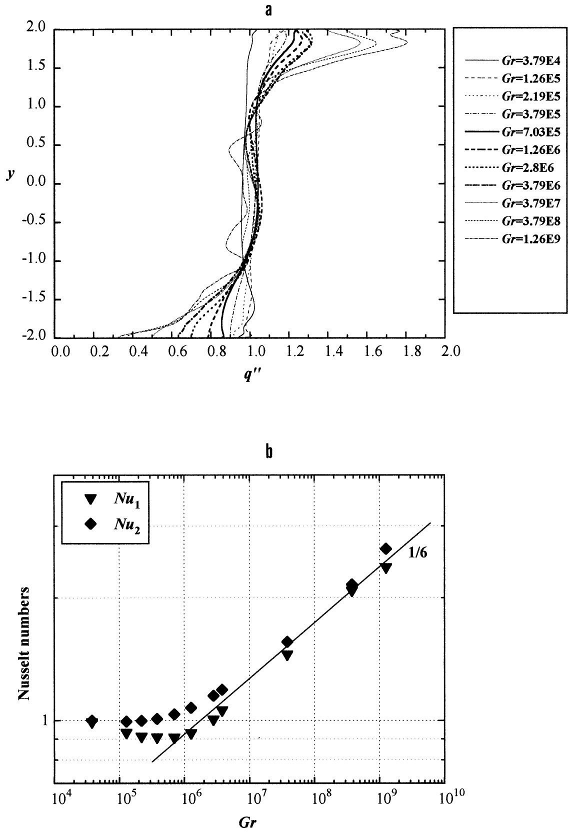

Fig. 24. Heat transfer (a) Time-averaged profiles of the wall heat flux q'' (normalized by its mean value $qD/2$) along the vertical walls for all cases investigated. The mean of left and right wall values is shown. (b) Dependence of the Nusselt numbers Nu_1 and Nu_2 upon the Grashof number.

For $Gr > \sim 10^6$, both Nu_1 and Nu_2 increase approximately as $Gr^{1/6}$. This behaviour differs from that ($Nu_2 \sim Gr^{0.23-0.24}$) indicated by the experimental results of Fiedler and Wille [8], Kulacki and Nagle [9], and by the computational studies of Farouk [13], and Dinh and Nourgaliev [15], which, however, refer to shallow layers cooled only from the upper surface and to a Prandtl number of 6–7. The lower Grashof number dependence found in the present study is coherent with the lower Prandtl number considered (0.0321); unfortunately, no results, either experimental or computational, have been described in the literature for the specific case of an internally heated low Prandtl number fluid.

12. Conclusions

A computational study was conducted of low-Prandtl number free convection in a volumetrically heated rectangular enclosure of aspect ratio 4, having adiabatic top and bottom walls and isothermal side walls. Direct numerical two-dimensional simulations were performed by a finite-volume method for Grashof numbers ranging from 3.79×10^4 to 1.26×10^9. According to the value of Gr, different flow regimes were obtained: steady-state, periodic, and chaotic. This suggests that, as Gr increases, the flow undergoes first a Hopf bifurcation, leading to a periodic regime, and then transition to chaos. The periodic regime exists only in a narrow range of Gr.

In all cases, the initial transient included the appearance and growth of two elongated, symmetric recirculation cells on the two sides of the cavity. At low values of Gr (up to $\sim 2 \times 10^5$), these cells remained stable and a steady-state configuration (base flow) was attained. In this range, the computed velocity and temperature distributions, away from the horizontal end walls of the cavity, were close to the theoretical solution for parallel flow. The velocity in the central rising plume and the downcoming boundary layers, as well as the shear stress, scaled linearly with the Grashof number.

Periodic solutions were obtained for $Gr = 3.79 \times 10^5$ and 7.03×10^5. In this range, the initial instability of the base flow was the growth of an antisymmetric velocity disturbance propagating downwards as a travelling wave having a dimensionless wavenumber of ~ 1 and a dimensionless speed of ~ 0.2. The Hopf bifurcation marking the transition from steady state to time-periodic flow was accompanied by the transition from symmetric to instantaneously asymmetric solutions (staggered rolls) with symmetric time averages.

For $Gr > \sim 10^6$, the flow periodicity was lost and chaotic solutions, exhibiting a broad-band spectrum, were obtained. Time series of monitoring quantities in the chaotic range, as well as instantaneous "snapshots" of the flow and temperature fields, clearly showed space and time-intermittence phenomena. Power spectra exhibited a low-frequency region associated with the renewal of rolls; a broad-band intermediate range characterized by a slope close to $-5/3$; and a steep fall at frequencies higher than a cutoff value. The latter depended upon the Grashof number and was associated with the dissipative scales of the chaotic motion.

Even in the chaotic range, the flow pattern took the form of downward-travelling staggered rolls and the dominating frequency was identifiable with the roll-renewal frequency, i.e. the frequency by which pairs of recirculation rolls were generated near the top corners of the cavity. Once made dimensionless, this was found to decrease in the periodic range, to increase as $Gr^{1/3}$ in the transitional range and to attain an almost uniform value of 0.25–0.30 in the fully chaotic range.

For sufficiently high Grashof numbers ($> 10^6$), the time-averaged Nusselt number (defined on the basis of the maximum or spatially averaged temperature) increased as $Gr^{1/6}$ and attained the relatively low value of ~ 2 at the highest Gr studied (1.26×10^9). The time-averaged wall friction coefficient decreased as $Gr^{-1/3}$.

The first transition from steady to periodic flow (Hopf bifurcation) followed qualitatively the predictions of linear stability theory for parallel flow in infinite-AR slots, but occurred at a Grashof number 3–4 times higher and resulted in slightly higher wavenumbers and lower wave speed; these discrepancies can all be explained by the finite height of the enclosure and the influence of the end walls. Linear stability analysis should be extended to finite-length enclosures before a quantitative comparison of theoretical and computational results can be drawn.

As regards the second transition from periodic to chaotic flow, we are not aware of the previous comparable studies, either analytical or numerical, for enclosures with internal heat generation. A theoretical analysis, which should probably be based on nonlinear stability theory, ought to focus on the basic mechanisms for the de-stabilization of the periodic travelling-roll pattern and on the possible existence of intermediate *quasi-periodic* regimes.

Of course, the present two-dimensional simulations leave unanswered the question of the stability of the flow under *three-dimensional* disturbances. The few available studies based on fully three-dimensional numerical simulations [30] suggest that free-convective flows in enclosures are more unstable with respect to three-dimensional than two-dimensional disturbances; therefore, it is possible that in three dimensions the boundaries between steady-state, periodic and chaotic regimes would be drastically different, and also that intermediate periodic solutions would *not* occur at all.

Finally, a better understanding of the influence of *aspect ratio* and *Prandtl number* on flow regimes and transitions would be highly desirable. The former aspect is currently being investigated by our group and will be discussed in future work.

References

[1] D.J. Tritton, M.N. Zarraga, Convection in horizontal layers with heat generation. Experiments, J. Fluid Mech 30 (1967) 21–32.

[2] E.L. Gluekler, L. Baker Jr., Post-accident heat removal in LMFBR's, in: O.C. Jones Jr., S.G. Bankoff (Eds.), Proc. Symp. on the Thermal and Hydraulic Aspects of Nuclear Reactor Safety, Liquid Metal Fast Breeder Reactors, vol. 2, ASME, New York, 1977, pp. 285–324.

[3] E. Proust, L. Anzidei, G. Casini, M. Dalle Donne, L. Giancarli, S. Malang, Breeding blanket for DEMO, Fusion Engng. and Des. 22 (1993) 19–33.

[4] W. Gudowski (Ed.), The Status of Accelerator-Driven Systems (ADS), IAEA, Vienna, 1999.

[5] F.A. Kulacki, D.E. Richards, Natural convection in plane layers and cavities with volumetric energy sources, in: S. Kakaç, W. Aung, R. Viskanta (Eds.), Natural Convection — Fundamentals and Applications, Hemisphere, New York, 1985, pp. 179–254.

[6] F.A. Kulacki, R.J. Goldstein, Thermal convection in a horizontal fluid layer with uniform volumetric energy sources, J. Fluid Mechanics 55 (1972) 271–287.

[7] M. Tveitereid, E. Palm, Convection due to internal heat sources, J. Fluid Mech 76 (1976) 481–499.

[8] Fiedler, H. and Wille, R., Wärmetransport bie frier Konvektion in einer horizontalen Flussigkeitsschicht mit Volumenheizung, Teil 1: Integraler Wärmetransport. Rep. Dtsch Forschungs-Varsuchsanstalt Luft-Raumfahrt, Inst. Turbulenzfenschung, Berlin (1971).

[9] F.A. Kulacki, M.E. Nagle, Natural convection in a horizontal fluid layer with volumetric energy sources, J. Heat Transfer 91 (1975) 204–211.

[10] F.A. Kulacki, A.A. Emara, Steady and transient thermal convection in a fluid layer with uniform volumetric energy sources, J. Fluid Mechanics 83 (1977) 375–395.

[11] A.G. Churbanov, P.N. Vabishchevich, V.V. Chudanov, V.F. Strizhov, A numerical study of natural convection of a heat generating fluid in rectangular enclosures, Int. J. Heat Mass Transfer 37 (1994) 2969–2984.

[12] P.G. Daniels, O.K. Jones, Convection in a shallow rectangular cavity due to internal heat generation, Int. J. Heat Mass Transfer 41 (1998) 3979–3987.

[13] B. Farouk, Turbulent thermal convection in an enclosure with internal heat generation, J. Heat Transfer 110 (1988) 126–132.

[14] V.A. Bui, T.N. Dinh, Prediction of turbulent characteristics in a fluid layer with internal energy sources, in: Proc. 2nd European Thermal-Sciences and 14th UIT National Heat Transfer Conference, 1996, pp. 1365–1372.

[15] T.N. Dinh, R.R. Nourgaliev, Prediction of turbulent characteristics in a fluid layer with internal energy sources, in: G.P. Celata, P. Di Marco, A. Mariani (Eds.), Proc. 2nd European Thermal-Sciences and 14th UIT National Heat Transfer Conference, ETS, Milan, 1996, pp. 843–850.

[16] T.N. Dinh, R.R. Nourgaliev, Turbulence modelling for large volumetrically heated liquid pools, Nucl. Engng. and Des. 169 (1997) 131–150.

[17] H.O. May, A numerical study on natural convection in an inclined square enclosure containing internal heat sources, Int. J. Heat Mass Transfer 34 (1991) 919–928.

[18] J.H. Lee, R.J. Goldstein, Experimental study on natural convection heat transfer in an inclined square enclosure containing internal energy sources, J. Heat Transfer 107 (1988) 855–866.

[19] S. Acharya, R.J. Goldstein, Natural convection in an externally heated vertical or inclined square box containing internal energy sources, J. of Heat Transfer 107 (1985) 855–866.

[20] T. Fusegi, J.M. Hyun, K. Kuwahara, Numerical study of natural convection in a differentially heated cavity with internal heat generation: effects of the aspect ratio, J. Heat Transfer 114 (1992) 773–777.

[21] Y.M. Shim, J.M. Hyun, Transient confined natural convection with internal heat generation, Int. J. Heat Fluid Flow 18 (1997) 328–333.

[22] M.G. Braunsfurth, A.C. Skeldon, A. Juel, T. Mullin, D.S. Riley, Free convection in liquid gallium, J. Fluid Mechanics 342 (1997) 295–314.

[23] K.H. Winters, Oscillatory convection in liquid metals in a horizontal temperature gradient, Int. J. Num. Meth. Engng. NSI (1988) 401–414.

[24] R. Viskanta, D.M. Kim, C. Gau, Three-dimensional natural convection heat transfer of a liquid metal in a cavity, Int. J. Heat Mass Transfer 29 (1986) 475–485.

[25] J.R. van Doormal, G.D. Raithby, Enhancements of the SIMPLE method for predicting incompressible flows, Numer. Heat Transfer 7 (1984) 147–163.

[26] M. Lèsieur, Turbulence in Fluids, Kluwer Academic Publisher, Amsterdam, 1990.

[27] R.A.W.M. Henkes, C.J. Hoogendoorn, Bifurcation to unsteady natural convection for air and water in a cavity heated from the side, in: Proc. 9th Int. Heat Tranfer Conf., Jerusalem, Israel, Aug. 19-24, 1990, pp. 57–262.

[28] C.J. Janssen, R.A.W. Henkes, Influence of Prandtl number on instability mechanisms and transition in differentially heated square cavity, J. Fluid Mechanics 290 (1995) 319–344.

[29] L.M. de Socio, L. Misici, A. Polzonetti, Natural Convection in Heat Generating Fluids in Cavities, ASME paper 79-HT-95 (1979).

[30] R.A.W.M. Henkes, P. Le Quéré, Three-dimensional transition of natural-convection flows, J. Fluid Mechanics 319 (1996) 281–303.